POLITECNICO DI TORINO
Repository ISTITUZIONALE

Geometrically nonlinear static analysis of multi-component structures through variable-kinematics finite elements

(Article begins on next page)

22 December 2024

ORIGINAL PAPER

R. Azzara · **E. Carrera** · **P. Chiaia** · **M. Filippi** · **A. Pagani** · **M. Petrolo** · **E. Zappino**

Geometrically nonlinear static analysis of multi-component structures through variable-kinematics finite elements

Abstract This paper presents a multi-dimensional variable-kinematics finite element model for nonlinear static analyses of structures with complex geometries. The approach incorporates higher-order beam models and classical solid finite elements in a unified framework, enabling refined modeling of complex geometries. The finite element procedure proposed follows the Carrera Unified Formulation (CUF) and uses a pure displacement-based methodology. The governing equations are derived within the classical continuum mechanics framework, and weak-form equilibrium equations are established using the Principle of Virtual Displacements (PVD). Within the CUF framework, higher-order beam and hexahedral solid models are defined in a unified manner, and the governing equations are written in terms of invariants of mathematical models used and the theory of structures approximation. A coupling technique is used between the beam and solid elements at the nodal level using superposition. The capabilities of fully nonlinear variable-kinematics models are investigated for the static analysis of various rectangular and curved structures. The numerical results are compared with solutions obtained using commercial software. Finally, the proposed methodology is applied to analyze more complex geometries in engineering applications. The results show the capabilities of variable-kinematics models in terms of both accuracy and computational efficiency for the computation of highly nonlinear deformed states and localized phenomena, such as stress concentrations and buckling.

1 Introduction

In today's engineering applications, various sectors such as civil, mechanical, aerospace, and automotive engineering demand that structures endure extreme conditions throughout their operational lifespan while

R. Azzara · E. Carrera · P. Chiaia · M. Filippi · A. Pagani · M. Petrolo (✉) · E. Zappino
MUL2 Lab, Department of Mechanical and Aerospace Engineering, Politecnico di Torino, Corso Duca degli Abruzzi 24, 10129 Turin, Italy
E-mail: marco.petrolo@polito.it

R. Azzara
E-mail: rodolfo.azzara@polito.it

E. Carrera
E-mail: erasmo.carrera@polito.it

P. Chiaia
E-mail: piero.chiaia@polito.it

M. Filippi
E-mail: matteo.filippi@polito.it

A. Pagani
E-mail: alfonso.pagani@polito.it

E. Zappino
E-mail: enrico.zappino@polito.it

maintaining nominal performance standards. Typically, the design of high-performance structures is conducted within the context of large displacements and rotations (geometrical nonlinearities) or nonlinear constitutive behaviour (material). Accurate predictions of complex structural behaviour, such as instabilities, localized phenomena, failure and damage, are crucial when composites, cross-ply laminates, and innovative materials enabled by advancements in manufacturing processes are considered. However, conducting physical tests on these components is often relatively expensive. Consequently, numerical simulation emerges as a helpful approach for analyzing the performance of innovative materials and structures. Moreover, it is nowadays a valuable tool for exploring novel topological features in the context of optimization problems [1].

Generally, the analysis of complex structures is performed via numerical methods based on the Finite Element Method (FEM). The FEM is a computationally efficient framework for its versatility and range of possible investigations. For brevity, readers are referred to [2–4] for a comprehensive description of this methodology. In the context of numerical simulations, the FEM has been extended in many structural applications ranging from classical linear problems to fully nonlinear problems such as large displacement/rotation regimes, progressive failure analysis, plasticity, and many others. Developing accurate and efficient FE procedures in nonlinear structural mechanics for analyzing materials and structures can be challenging due to well-known mathematical and numerical limitations.

The FEM enables the analysis of structures through elementary elements formulated under kinematic and constitutive assumptions. One-dimensional (1D) beam, two-dimensional (2D) plate/shell, or three-dimensional (3D) solid elements are defined within the framework of classical continuum mechanics. Typically, the kinematic assumptions for each element are based on well-established structural theories, including those formulated by Euler [5] and Timoshenko [6] for beams, by Love [7], Reissner [8], and Mindlin [9] for plates and shells. Although computationally advantageous, adopting FE models based on these classical structural theories generally leads to inaccurate and inconsistent solutions when dealing with nonlinear problems [10–12]. In general, the most accurate solution to the governing equilibrium equations is given by adopting 3D elements that allow a direct discretization of the discrete unknown variables of the equilibrium equations without any kinematic assumption on the structural theory. However, employing 3D elements significantly increases the computational costs in many cases, e.g., when dealing with thin-walled structures or ultra-thin composite laminates.

To simulate complex structures, adopting 1D, 2D, and 3D elements simultaneously in the same model can lead to a more efficient approach, providing accurate results with an acceptable computational cost required by the numerical simulation. Over the years, various coupling techniques were introduced to ensure accuracy and efficiency. Argiris and Kelsey [13] proposed the force method to provide solutions to elastic problems. Surana [14] proposed an approach to connect solid and plate elements. Liao [15] presented the coupling between solid and shell elements. Cofer and Will developed the same coupling [16], while Gmür and Schorderet provided the connection between 1D and 3D elements [17]. A mixed-dimensional coupling method, based on geometrical assumptions, was developed by McCune et al. [18]. Song [19] adopted an asymptotic approach to join solids and beams. For completeness, the reader is referred to [20–22] for other interesting approaches that use multi-dimensional models.

The classical FE formulations may be inadequate for analyzing highly nonlinear phenomena. Euler-Bernoulli Beam Theory (EBBT) or Timoshenko Beam Theory (TBT) exploit a-priori displacement fields with lower-order expressions of the strain components that can consequently limit the overall accuracy of the model and lead to inconsistent solutions [23]. On the other hand, hexahedral 3D FE models suffer from decreased accuracy due to locking phenomena arising from lower-order formulations and aspect-ratio constraints in the discretization definition. Instead, adopting higher-order structural theories is beneficial when large deformation regimes, cross-section warping, twisting, and other local deformations are under investigation or complex stress states are required. In recent years, higher-order FE models have been developed within the well-established Carrera Unified Formulation (CUF) framework to address static and dynamic analysis of complex structures. Higher-order beam, plate/shell, and hexahedral models based on the CUF have demonstrated their efficacy and accuracy in various applications, see [24–26]. The CUF offers a unified framework for deriving FE models with variable kinematics, regardless of the specific theory of structural approximation employed. Within this framework, the governing equations are written in terms of invariants the kinematic model and structural theory adopted, thanks to the hierarchical formalism adopted. Refined 1D, 2D, and 3D models are derived by adopting the same mathematical formalism without loss of generality, implementing any higher-order structural theories to overcome the limitations of classical theories. Furthermore, thanks to this key feature, a consistent coupling technique of different variable-kinematics models has been developed in recent years and assessed considering the modal analysis of complex aircraft structures [27] and thin-walled
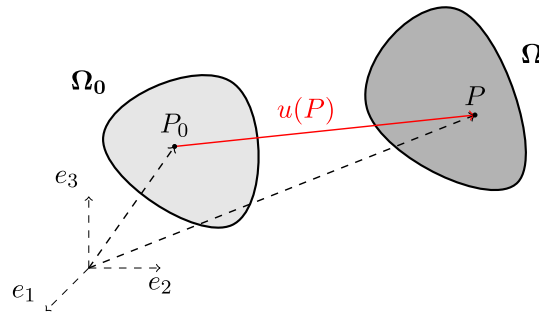
Fig. 1 Reference and actual configuration of a deformable body

reinforced structures [28], the modelling of composites helicopter blades [29] and free-edge analysis of laminated composites [30]. This work aims to extend variable-kinematic models to the geometrically nonlinear static analysis of structures. The following presents a pure displacement-based FE model for studying complex structures using unified 1D beam models and classical 3D hexahedral models defined in the CUF framework. In addition, the coupling technique of variable-kinematics elements is presented to describe the procedure adopted for local mathematical model refinements, the definition of multi-dimensional models, and the development of a novel efficient numerical tool in nonlinear structural mechanics.

This article is organized as follows: (i) Sect. 2 provides the theoretical background in the continuum mechanics framework, including the definition of higher-order 1D beam and classical 3D solid finite element models both exploited in the CUF framework; (ii) the derivation of weak-form governing equations and finite element procedures implemented are described in Sect. 3, explicitly reporting the derivation of Fundamental Nuclei (FN) of FE matrices and the iterative-incremental numerical solver adopted; (iii) different benchmark cases to assess the capabilities of the proposed finite element modelling and coupling techniques are presented in Sect. 4, comparing numerical results obtained by the present implementation of variable-kinematics models with reference solutions; (iv) finally, the main conclusions are discussed in Sect. 5.

2 Structural theories and finite elements

This section presents the theoretical framework that has been developed, along with the variable-kinematics finite element models based on CUF. The formulation of the static nonlinear problem is carried out within the classical continuum mechanics framework. The governing equations are written in a compact matrix representation, thereby enabling the definition of the proposed displacement-based FE model independently of the mathematical model adopted. Subsequently, the same unified formalism defines higher-order beam models and classical hexahedral solid FE models. Furthermore, the variable kinematic technique is presented, allowing for combining 1D and 3D models. Within the CUF framework, this technique eliminates the need for ad-hoc coupling procedures, ensuring a seamless integration of the different models.

2.1 Displacement, strain and stress fields

Let us consider a continuum body in the 3D space. Figure 1 shows the Cartesian reference frame $\Sigma = \{\mathbf{e}_1, \mathbf{e}_2, \mathbf{e}_3\}$, the material reference configuration $\boldsymbol{\Omega}_0$ and actual deformed configuration $\boldsymbol{\Omega}$ of the continuum body.

For a generic material point of the continuum body located at coordinates (x, y, z) with respect to Σ reference frame, the lagrangian displacement field is defined as follows:

$$\mathbf{u}(x, y, z) = \{\, u_x(x, y, z), u_y(x, y, z), u_z(x, y, z) \,\}^{\mathrm{T}} \tag{1}$$

In the present work, the strain stems from the full Green-Lagrange strain tensor, denoted as $\boldsymbol{\varepsilon}$. By adopting the Voigt's notation for symmetric tensorial quantities, the strain tensor is written as follows:

$$\boldsymbol{\varepsilon}(x, y, z) = \{\, \varepsilon_{xx}, \varepsilon_{yy}, \varepsilon_{zz}, \varepsilon_{xz}, \varepsilon_{yz}, \varepsilon_{xy} \,\}^{\mathrm{T}} \tag{2}$$

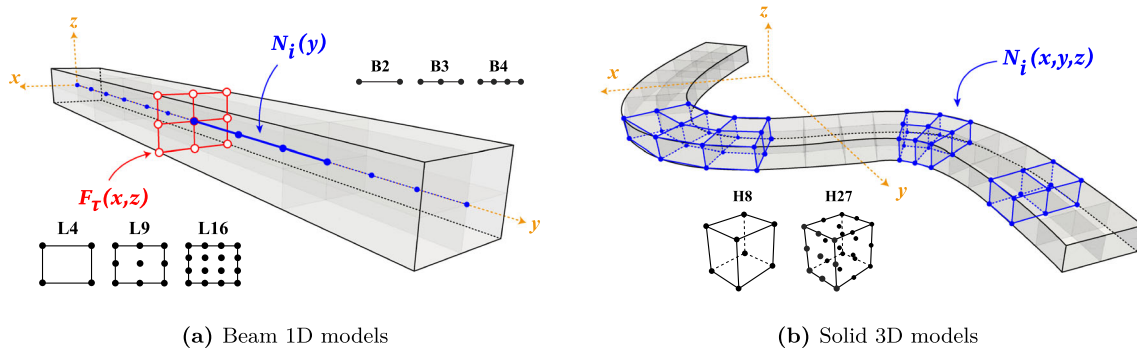(a) Beam 1D models   (b) Solid 3D models

Fig. 2 Geometrical representation of CUF-based FE models

In this work, the stress–strain relation, namely the constitutive law, is written in compact form adopting Hooke's law for linear elastic materials:

$$\boldsymbol{\sigma} = \mathbb{C}\boldsymbol{\varepsilon} \tag{3}$$

in which the Cauchy's stress tensor is defined following Voigt's notation:

$$\boldsymbol{\sigma}(x, y, z) = \{\, \sigma_{xx}, \sigma_{yy}, \sigma_{zz}, \sigma_{xz}, \sigma_{yz}, \sigma_{xy} \,\}^{\mathrm{T}} \tag{4}$$

2.2 One- and three-dimensional models via the Carrera Unified Formulation

In the CUF framework, the generic 3D displacement field is provided as a polynomial expansion of the generalized nodal displacements by employing the theory of structure approximations. The unified formulation of higher-order 1D CUF models for the geometrically nonlinear static analysis of beam structures is presented in [31]. Instead, the formulation of hexahedral solid models in CUF for the geometrical and material nonlinear analysis has been recently introduced by [32]. In the classical orthonormal $\{x, y, z\}$ Cartesian reference frame, the displacement field **u** is written, under the unified approach, as:

$$\text{Beam 1D models: } \mathbf{u}(x, y, z) = F_\tau(x, z)N_i(y)\mathbf{u}_{\tau i} \; \tau = 1, ..., M, \; i = 1, ..., N_n^{1\mathrm{D}} \tag{5}$$

$$\text{Solid 3D models: } \mathbf{u}(x, y, z) = 1 \cdot N_i(x, y, z)\mathbf{u}_{\tau i} \; \tau = 1, \quad i = 1, ..., N_n^{3\mathrm{D}} \tag{6}$$

where F_τ is the set of the cross-section expansion basis adopted representing the theory of structures approximation, N_i is the set of Lagrange polynomials defined, respectively, by the total number of nodes $N_n^{1\mathrm{D}}$ considered in the 1D beam axis discretization model and 3D model $N_n^{3\mathrm{D}}$ nodes. $\mathbf{u}_{\tau i}$ indicates the vector of generalized unknown displacement components. A higher-order 1D beam model is uniquely characterized by the choice of the cross-section expansion functions F_τ and the order of the cross-section kinematics expansion M. Figure 2 shows the graphical representation of the unified 1D CUF model and general 3D hexahedral model. In the present work, a variable-kinematics finite element coupling technique is proposed for models based on Lagrange-type expansion models; thus, F_τ corresponds to the set of 2D Lagrange polynomials having as generalized unknowns, $\mathbf{u}_{\tau i}$, pure displacement components.

2D and 3D Lagrange polynomials, used respectively for the beam cross-section discretization and full 3D solid FE model, are defined in the natural reference frame, exploiting the isoparametric formulation. The reader is referred to [33] for the explicit expressions of linear, parabolic, and cubic Lagrange polynomials. In the case of solid finite elements, the mathematical model is entirely characterized by the total number of nodes involved in the definition $N_n^{3\mathrm{D}}$, since the basis of CUF expansion functions is set to $F_\tau = 1$, even so, the definition of 3D displacement field is included in the unified approach and can be exploited regardless. Figures 3 and 4 show the definition of linear 1D expansion L4 (four-node) and linear 3D H8 (eight-node) finite elements and their transformation to the natural reference frames. Higher-order 1D beam models will be discussed, specifically referring to the finite element approximation of the beam axis using linear (B2), parabolic (B3), and cubic (B4) models. Additionally, the cross-section expansion elements will be denoted as four-node linear (L4), nine-node parabolic (L9), and quadratic six-node cubic (L16). In the case of fully 3D hexahedral models, the standard tri-linear hexahedral model (H8) and tri-parabolic hexahedral model (H27) will be adopted.
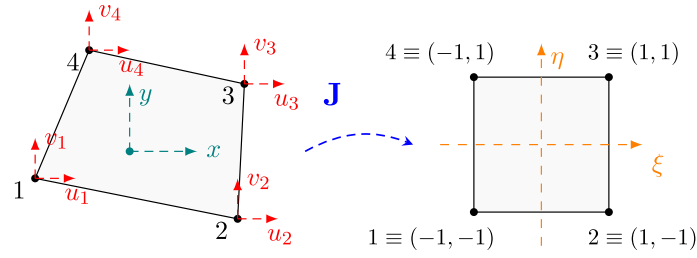
Fig. 3 Lagrange L4 linear expansion model: from material to natural reference frame
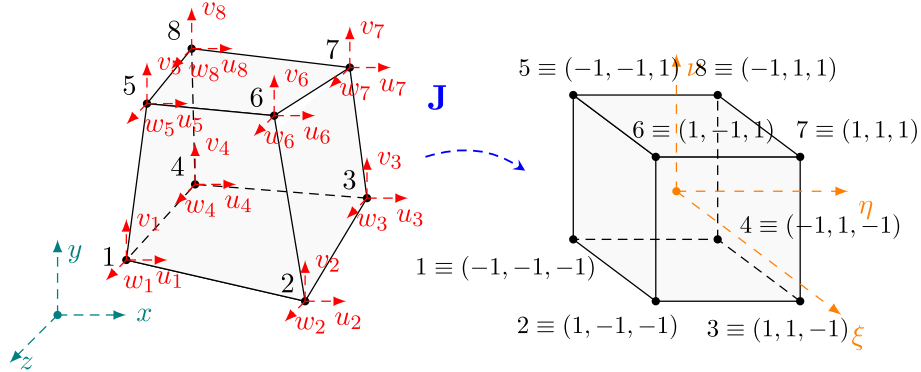

Fig. 4 Lagrange H8 tri-linear finite element: from material to natural reference frame

The adoption of LE models, as reported in [34], allows the definition of independent displacement field discretizations to different structure sub-components. This approach, allowed by CUF, has also been called the Component-Wise (CW) approach. Then, the independent displacement fields are coupled, imposing the continuity of displacement components at nodal level, leveraging on the physical meaning of the generalized unknowns of 1D beam models. To exploit the proposed CW approach also in variable-kinematics FE models, the classical 3D FE formulations have been rewritten in the unified framework for the purposes of the present work in multi-dimensional models for the large displacement analysis of structures.

3 Governing equations

3.1 Internal and external forces vectors

In the present work, the weak-form of the governing equations is exploited through the Principle of Virtual Displacements (PVD). Under the hypothesis of negligible body forces, the PVD is written as follows:

$$\delta\mathcal{L}_{int} = \delta\mathcal{L}_{ext} \tag{7}$$

where $\delta\mathcal{L}_{int}$ is the virtual variation of internal strain energy stored during the deformation process, and $\delta\mathcal{L}_{ext}$ is the virtual variation of the work of external loads done by virtual displacements.

$$(a)\ \delta\mathcal{L}_{int} = \int_{\Omega} \delta\boldsymbol{\varepsilon}^{\mathrm{T}}\boldsymbol{\sigma}\, dV \qquad (b)\ \delta\mathcal{L}_{ext} = \int_{\Omega} \delta\boldsymbol{u}^{\mathrm{T}}\mathbf{f}\, dV \tag{8}$$

where $\boldsymbol{\varepsilon}$ is the full Green-Lagrange strain tensor, $\boldsymbol{\sigma}$ is the Cauchy's stress tensor, $\mathbf{f}$ is the vector of external loads, the symbol δ denotes the virtual variation. In the present work, finite element models are defined in a Total Lagrangian (TL) approach; subsequently, all volume integrals are referred to the material (or reference) configuration. The generic virtual displacement field for a finite element defined under CUF is then rewritten as:

$$\delta\mathbf{u} = F_s\delta\mathbf{u}_s = F_s N_j\delta\mathbf{u}_{sj}\ \ j = 1, .., N_n,\ s = 1, ..., M\ \rightarrow\ \begin{cases} \text{1D: } \delta\mathbf{u}(x, y, z) = F_s(x, z)N_j(y)\delta\mathbf{u}_{sj} \\ \text{3D: } \delta\mathbf{u}(x, y, z) = 1_s \cdot N_j(x, y, z)\delta\mathbf{u}_{sj} \end{cases} \tag{9}$$

Again, in the case of 3D hexahedral models, the set of expansion basis functions for the virtual displacement field is set to $F_s = 1$. Regarding the fully nonlinear geometrical relations, in the present work the strain measure adopted is the full Green-Lagrange strain tensor, rewritten in compact form as in Pagani and Carrera [31]:

$$\boldsymbol{\varepsilon} = (\mathbf{b}_l + \mathbf{b}_{nl})\mathbf{u} = (\mathbf{b}_l + \mathbf{b}_{nl})F_\tau N_i \mathbf{u}_{\tau i} = (\mathbf{B}_l^{\tau i} + \mathbf{B}_{nl}^{\tau i})\mathbf{u}_{\tau i} \tag{10}$$

obtaining the definition of algebraic matrices $\mathbf{B}_l^{\tau i}$ and $\mathbf{B}_{nl}^{\tau i}$, whose formal expression are independent of the theory of structure approximation and finite element model adopted; e.g., for the beam case the matrices are:

$$\mathbf{B}_l^{\tau i} = \begin{bmatrix} F_{\tau,x} N_i & 0 & 0 \\ 0 & F_\tau N_{i,y} & 0 \\ 0 & 0 & F_{\tau,z} N_i \\ F_{\tau,z} N_i & 0 & F_{\tau,x} N_i \\ 0 & F_{\tau,z} N_i & F_\tau N_{i,y} \\ F_\tau N_{i,y} & F_{\tau,x} N_i & 0 \end{bmatrix} \tag{11}$$

$$\mathbf{B}_{nl}^{\tau i} = \frac{1}{2}\begin{bmatrix} u_{x,x} F_{\tau,x} N_i & u_{y,x} F_{\tau,x} N_i & u_{z,x} F_{\tau,x} N_i \\ u_{x,y} F_\tau N_{i,y} & u_{y,y} F_\tau N_{i,y} & u_{z,y} F_\tau N_{i,y} \\ u_{x,z} F_{\tau,z} N_i & u_{y,z} F_{\tau,z} N_i & u_{z,z} F_{\tau,z} N_i \\ u_{x,x} F_{\tau,z} N_i + u_{x,z} F_{\tau,x} N_i & u_{y,x} F_{\tau,z} N_i + u_{y,z} F_{\tau,x} N_i & u_{z,x} F_{\tau,z} N_i + u_{z,z} F_{\tau,x} N_i \\ u_{x,y} F_{\tau,z} N_i + u_{x,z} F_\tau N_{i,y} & u_{y,y} F_{\tau,z} N_i + u_{y,z} F_\tau N_{i,y} & u_{z,y} F_{\tau,z} N_i + u_{z,z} F_\tau N_{i,y} \\ u_{x,x} F_\tau N_{i,y} + u_{x,y} F_{\tau,x} N_i & u_{y,x} F_\tau N_{i,y} + u_{y,y} F_{\tau,x} N_i & u_{z,x} F_\tau N_{i,y} + u_{z,y} F_{\tau,x} N_i \end{bmatrix} \tag{12}$$

The explicit expression of these matrices for the 3D solid models can be found in [32]. The virtual variation of the Green-Lagrange strain tensor is carried out by adopting the discretization of virtual displacement field, Eq. (9):

$$\delta\boldsymbol{\varepsilon} = \delta((\mathbf{B}_l^{\tau i} + \mathbf{B}_{nl}^{\tau i})\mathbf{u}_{\tau i}) = (\mathbf{B}_l^{sj} + 2\mathbf{B}_{nl}^{sj})\delta\mathbf{u}_{sj} \tag{13}$$

Assuming Eqs. (10)–(13) for the real and virtual strain measures, the virtual variation of the internal work is then exploited and written for a linear elastic material as follow:

$$\begin{aligned} \int_\Omega \delta\boldsymbol{\varepsilon}^{\mathrm{T}}\boldsymbol{\sigma}\,dV &= \int_\Omega \delta\mathbf{u}_{sj}^{\mathrm{T}}(\mathbf{B}_l^{sj} + 2\mathbf{B}_{nl}^{sj})^{\mathrm{T}}\mathbb{C}(\mathbf{B}_l^{\tau i} + \mathbf{B}_{nl}^{\tau i})\mathbf{u}_{\tau i}\,dV \\ &= \delta\mathbf{u}_{sj}^{\mathrm{T}}\mathbf{K}_{ll}^{\tau sij}\mathbf{u}_{\tau i} + \delta\mathbf{u}_{sj}^{\mathrm{T}}\mathbf{K}_{lnl}^{\tau sij}\mathbf{u}_{\tau i} + \delta\mathbf{u}_{sj}^{\mathrm{T}}\mathbf{K}_{nll}^{\tau sij}\mathbf{u}_{\tau i} + \delta\mathbf{u}_{sj}^{T}\mathbf{K}_{nlnl}^{\tau sij}\mathbf{u}_{\tau i} \\ &= \delta\mathbf{u}_{sj}^{\mathrm{T}}\mathbf{K}_S^{\tau sij}\mathbf{u}_{\tau i} \end{aligned} \tag{14}$$

where $\mathbf{K}_S^{\tau sij}$ is the 3x3 Fundamental Nucleus (FN) of the secant stiffness matrix, obtained as the sum of the linear stiffness matrix, $\mathbf{K}_{ll}^{\tau sij}$, and the nonlinear FN contributions $\mathbf{K}_{lnl}^{\tau sij}$, $\mathbf{K}_{nll}^{\tau sij}$ and $\mathbf{K}_{nlnl}^{\tau sij}$. The FN is the building block of the finite element matrices and is invariant with respect to the structural theory and finite element discretization adopted. Following the same derivation procedure, the work done by external forces is defined as:

$$\delta\mathcal{L}_{ext} = \int_\Omega \delta\boldsymbol{u}^{\mathrm{T}}\mathbf{f}\,dV = \int_\Omega \delta\mathbf{u}_{sj}^{\mathrm{T}}F_s N_j\mathbf{f}\,dV = \delta\mathbf{u}_{sj}^{\mathrm{T}}\mathbf{F}_{ext}^{sj} \tag{15}$$

where $\mathbf{F}_{ext}^{sj}$ is the 3×1 FN of the external loads vector. Each FN of the secant stiffness matrix and external forces vector are defined independently of the kinematic model and theory of structure approximation adopted in the finite element displacement field definition. As a result, the derived expressions are applicable regardless of the polynomial expansions adopted in the displacement field definition. The FN are uniquely determined by employing the corresponding definitions of finite element shape functions denoted as N_i, N_j for beam axis and solid hexahedral nodes, and the theory of structure approximation denoted as F_τ and F_s for beam cross-section of any order. By assembling the global secant stiffness matrix $\mathbf{K}_S$ and external load vector $\mathbf{F}_{ext}$ through summation over indices τ, s, i and j, the PVD is written in compact notation as follows:

$$\mathbf{K}_S\mathbf{u} = \mathbf{F}_{ext} \tag{16}$$

3.2 Linearization of governing equations

Due to the presence of geometrical nonlinearities, the static problem Eq. (16) is a nonlinear algebraic set of equations that has to be solved iteratively, adopting incremental solvers. The equilibrium condition is then rewritten as an equivalent minimization problem of residual nodal forces vector [35]:

$$\boldsymbol{\varphi}_{res} = \mathbf{K}_S \mathbf{u} - \mathbf{F}_{ext} = 0 \tag{17}$$

This work implements a Newton–Raphson linearized iterative scheme. In the incremental procedure, a first-order Taylor expansion of the residual forces vector around a known condition $(\mathbf{u}^0, \mathbf{F}_{ext}^0)$ is considered:

$$\boldsymbol{\varphi}_{res}(\mathbf{u}^0 + \Delta\mathbf{u}, \mathbf{F}_{ext} + \Delta\mathbf{F}_{ext}) = \boldsymbol{\varphi}_{res}(\mathbf{u}^0, \mathbf{F}_{ext}^0) + \frac{\partial\boldsymbol{\varphi}_{res}}{\partial\mathbf{u}}\Delta\mathbf{u} + \frac{\partial\boldsymbol{\varphi}_{res}}{\partial\mathbf{F}_{ext}}\Delta\lambda \cdot \mathbf{F}_{ext}^{rif} \tag{18}$$

where the finite variation of the external load vector is exploited utilizing the conservative load hypothesis [31], introducing the additional variable λ, the load-scale factor. The tangent stiffness matrix is defined following the classical approach $\frac{\partial\boldsymbol{\varphi}_{res}}{\partial\mathbf{u}} = \mathbf{K}_T$. Finally, supposing that the incremental solution is an equilibrium condition, namely, $\boldsymbol{\varphi}_{res}(\mathbf{u}^0 + \Delta\mathbf{u}, \mathbf{F}_{ext} + \Delta\mathbf{F}_{ext}) = 0$, one may write the final linear system of equations for the increment of unknown variables, that has to be coupled with an additional constraint equation to close algebraically the problem:

$$\begin{cases} \mathbf{K}_T(\mathbf{u}^0)\Delta\boldsymbol{u} = \Delta\lambda\mathbf{F}_{ext}^{ref} - \boldsymbol{\varphi}_{res}(\mathbf{u}^0, \mathbf{F}_{ext}^0) \\ c(\Delta\mathbf{u}, \Delta\lambda) = 0 \end{cases} \tag{19}$$

The constraint equation characterizes the numerical scheme adopted. It can be a displacement control, a load control, or a path-following method by adopting a different constraint. The present work adopts the path-following method proposed by Crisfield [36]. Readers are referred to [31,35,37] for detailed information about this method.

3.3 Tangent stiffness matrix

The tangent stiffness matrix is used in the linearized equation, Eq. (19). In the following, the explicit expression of the tangent matrix is carried out by considering the linearization of the internal strain energy. The CUF approach leading to the definition of the fundamental nucleus remains valid, i.e., the fundamental nucleus of the tangent stiffness matrix is invariant with respect to the structural theory and the finite element discretization,

$$\Delta(\delta\mathcal{L}_{int}) = \int_\Omega \Delta(\delta\boldsymbol{\varepsilon}^{\mathrm{T}}\boldsymbol{\sigma})dV = \int_\Omega \delta\boldsymbol{\varepsilon}^{\mathrm{T}}\Delta\boldsymbol{\sigma}\,dV + \int_\Omega \Delta(\delta\boldsymbol{\varepsilon}^{\mathrm{T}})\boldsymbol{\sigma}\,dV \tag{20}$$

The first term is related to the linearization of the constitutive equation. Under the assumption of linear elastic constitutive law, or constant elasticity tensor, the finite variation of the stress adopted is rewritten as:

$$\Delta\boldsymbol{\sigma} = \Delta(\mathbb{C}\boldsymbol{\varepsilon}) = \mathbb{C}\Delta\boldsymbol{\varepsilon} = \mathbb{C}(\mathbf{B}_l^{\tau i} + 2\mathbf{B}_{nl}^{\tau i})\Delta\mathbf{u}_{\tau i} \tag{21}$$

Thus, the first term in the linearized expression of the PVD is:

$$\begin{aligned} \int_\Omega \delta\boldsymbol{\varepsilon}^{\mathrm{T}}\Delta\boldsymbol{\sigma}\,dV &= \int_\Omega \delta\mathbf{u}_{sj}^{\mathrm{T}}(\mathbf{B}_l^{sj} + 2\mathbf{B}_{nl}^{sj})^{\mathrm{T}}\mathbb{C}(\mathbf{B}_l^{\tau i} + 2\mathbf{B}_{nl}^{\tau i})\Delta\mathbf{u}_{\tau i}\,dV \\ &= \delta\mathbf{u}_{sj}^{\mathrm{T}}\mathbf{K}_{ll}^{\tau sij}\Delta\mathbf{u}_{\tau i} + \delta\mathbf{u}_{sj}^{\mathrm{T}}2\mathbf{K}_{lnl}^{\tau sij}\Delta\mathbf{u}_{\tau i} + \delta\mathbf{u}_{sj}^{\mathrm{T}}\mathbf{K}_{nll}^{\tau sij}\Delta\mathbf{u}_{\tau i} + \delta\mathbf{u}_{sj}^{T}2\mathbf{K}_{nlnl}^{\tau sij}\Delta\mathbf{u}_{\tau i} \\ &= \delta\mathbf{u}_{sj}^{\mathrm{T}}\mathbf{K}_{ll}^{\tau sij}\Delta\mathbf{u}_{\tau i} + \delta\mathbf{u}_{sj}^{\mathrm{T}}\mathbf{K}_{T_1}^{\tau sij}\Delta\mathbf{u}_{\tau i} \end{aligned} \tag{22}$$

where $\mathbf{K}_{T_1}^{\tau sij} = 2\mathbf{K}_{lnl}^{\tau sij} + \mathbf{K}_{nll}^{\tau sij} + 2\mathbf{K}_{nlnl}^{\tau sij}$ is the contribution given by the linearization of the constitutive law. The second term of Eq. (20) is the FN of the geometrical stiffness matrix $\mathbf{K}_\sigma^{\tau sij}$, stemming from the linearization of geometrical relations:

$$\int_\Omega \Delta(\delta\boldsymbol{\varepsilon})^{\mathrm{T}}\boldsymbol{\sigma}\,dV = \delta\mathbf{u}_{sj}^{\mathrm{T}}\mathbf{K}_\sigma^{\tau sij}\Delta\mathbf{u}_{\tau i} \tag{23}$$
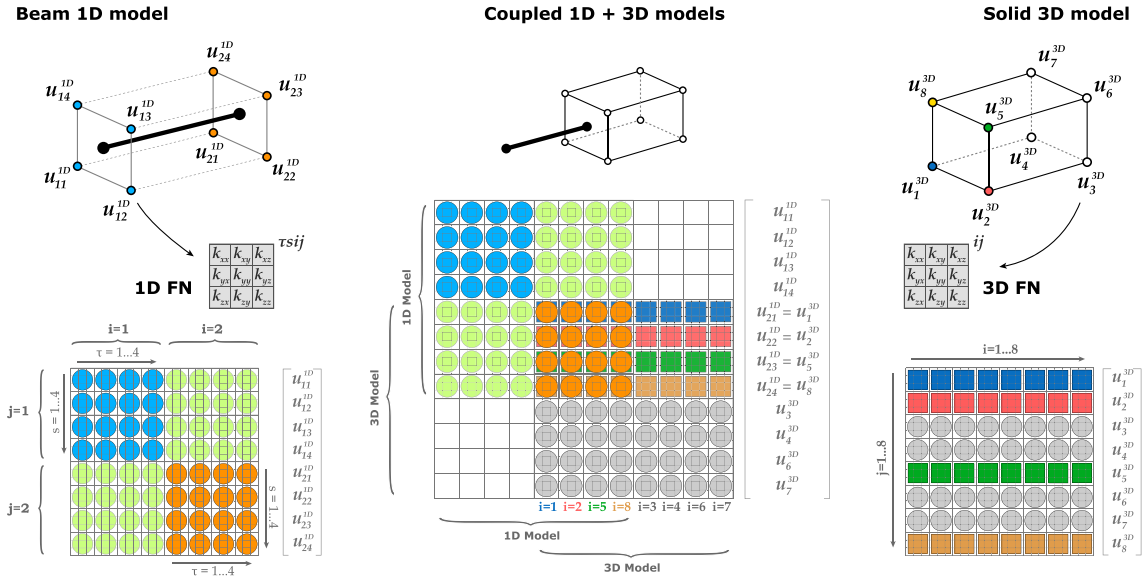
Fig. 5 Coupled 1D-3D models: assembling procedure

Finally, by substituting the expression of the contribution coming from the linearization of the constitutive equation, Eq. (14), and the one coming from the linearization of the geometrical relations, Eq. (23), the FN of the tangent stiffness matrix is defined as follows:

$$\Delta(\delta\mathcal{L}_{int}) = \int_\Omega \delta\boldsymbol{\varepsilon}^{\mathrm{T}}\Delta\boldsymbol{\sigma}\,dV + \int_\Omega \Delta(\delta\boldsymbol{\varepsilon})^{\mathrm{T}}\boldsymbol{\sigma}\,dV$$
$$= \delta\mathbf{u}_{sj}^{\mathrm{T}}\mathbf{K}_{ll}^{\tau sij}\Delta\mathbf{u}_{\tau i} + \delta\mathbf{u}_{sj}^{\mathrm{T}}\mathbf{K}_{T_1}^{ij}\Delta\mathbf{u}_{\tau i} + \delta\mathbf{u}_{sj}^{\mathrm{T}}\mathbf{K}_{\sigma}^{\tau sij}\Delta\mathbf{u}_{\tau i}$$
$$= \delta\mathbf{u}_{sj}^{\mathrm{T}}\mathbf{K}_{T}^{\tau sij}\Delta\mathbf{u}_{\tau i} \tag{24}$$

3.4 Assembling procedure of multi-dimensional models

The variable-kinematics models, introduced by Zappino and Carrera [38] and now extended to the geometrically nonlinear analysis of structures, are pure displacement-based finite element models. The unknowns of the model, namely the degrees of freedom (DOF), are the physical displacement components of each node. This property allows the coupling of different finite element models with different kinematics or theory of structure approximation independently of the refined mathematical formulation adopted. The assembling procedure is obtained by imposing the equivalence of displacement components at corresponding nodes commonly shared between two different models. In the case of merging nodes from two different finite element models, the fundamental nuclei of the stiffness matrices previously introduced are superimposed and combined in the assembling procedure of the global physical FE matrices like the tangent stiffness matrix or the internal force vector. Figure 5 shows the variable-kinematics assembling procedure of refined 1D beam models and hexahedral 3D models in terms of FE matrices assembling procedure. The adoption of LE models in the cross-section expansion of the beam structure with higher-order 1D CUF models allows the straightforward assembling procedure thanks to the geometrical meaning of the DOF involved in the mathematical 1D model.

Thanks to the proposed approach, the assembly procedures ensure the straightforward coupling between variable-kinematics finite elements. This allows 1D beam models, based on higher-order structural theories, to be connected at the nodal level with classical 3D elements. Consequently, in complex geometries, local refinements with higher-order beam models are used, overcoming the limitations of classical beam theories, such as rigid cross-section, incompatibility of transverse normal and shear stresses at beam edges, or constant shear stress along the cross-section. Exploiting the CUF formalism, no ad-hoc coupling techniques are required, e.g., Lagrange's multipliers. The proposed coupling procedure acts at the nodal level; thus, a 3D discretization model and a 1D cross-section expansion model are selected considering the superposition of common nodes.
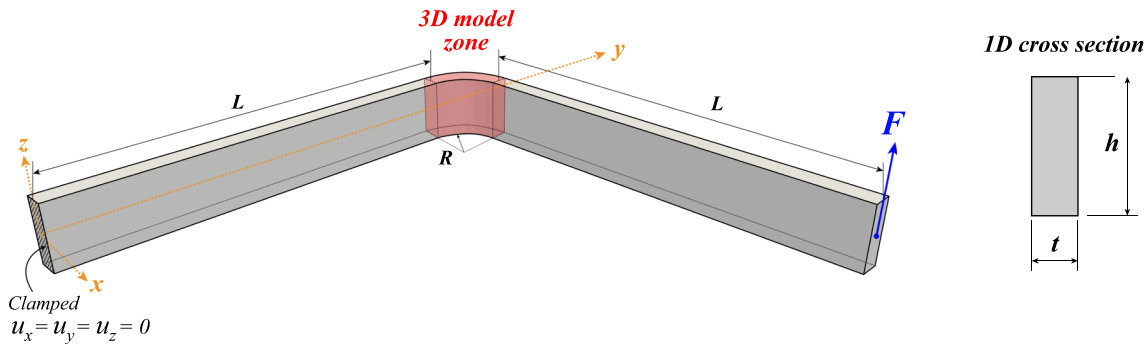
Fig. 6 Clamped angle frame: geometry and multi-dimensional discretization adopted

Even if the displacement field is continuous at each interface, local concentrations and oscillations of the stress field may arise in the transition zone because of the introduced coupling as discussed in [38].

4 Numerical results

In this section, numerical results are presented and verified, adopting benchmark problems available in literature or commercial codes as reference results. This work investigates different case studies, showing the capabilities of the proposed variable-kinematics models when complex geometries are analyzed.

4.1 Clamped rectangular frame subjected to shear load

The first case is a clamped angle frame, where a curved connecting zone is considered. Figure 6 shows the geometrical features and boundary conditions considered: two straight frames, with length $L = 200$ mm and cross-section dimensions $t = 10$ mm and $h = 30$ mm, are connected with a curved 90° corner with internal radius $R = 20$ mm. The frame is made of aluminum, and the material constants considered are $E = 70$ GPa and $\nu = 0.3$. The discretization models adopted employ 1D beam finite elements for the two straight sides and hexahedral 3D models for the corner. Different cross-section expansion models will be considered, adopting N_h L9 element along the lateral side and N_{B4} finite elements along the beam axis. The corner is discretized adopting $N_h \times N_{tan}$ H27 hexahedral parabolic finite elements, where N_h is the total number of elements along the radial direction and N_{tan} instead along the tangential curved direction. Figure 7 shows the discretization adopted and the variable-kinematics assembly. The frame is considered clamped at one end and subjected to a vertical out-of-plane concentrated load applied to the center of the free end.

The convergence analysis investigates the influence of beam axis kinematics, the cross-section expansion models and the 3D discretization adopted for the corner. The proposed model results are compared with a numerical solution obtained by a fully 3D model analyzed by ABAQUS commercial software. The accuracy and the efficiency of the proposed approach will be analyzed by comparing the computational cost required by the simulation and the relative difference between the proposed solutions. Tables 1 and 2 show the comparison between displacement components computed by variable-kinematics models when different values of the shear load are considered, comparing the results with the reference solution; the number of degrees of freedom of each model is reported in the last column and the relative errors between the proposed results and the reference are reported in brackets. Figure 8 shows the equilibrium paths measuring the displacement components at the point-load application, obtained by 20 N_{B4} B4 elements and considering the previously indicated cross-section expansion models and 3D hexahedral models.

The results suggest that:

- The convergence analysis proposed for the out-of-plane load case shows accurate displacement component u_z and u_x predictions for each adopted mathematical model. In particular, regarding the out-of-plane component u_z, accurate results are observed in all displacement regimes, differently with respect to the component u_x, for which coarser discretization does not match perfectly the reference solution at the low displacement regimes. The problem analyzed is highly nonlinear at small load values; moderate discrepancies, less than 5%, are observed. Similar considerations are addressed regarding the convergence
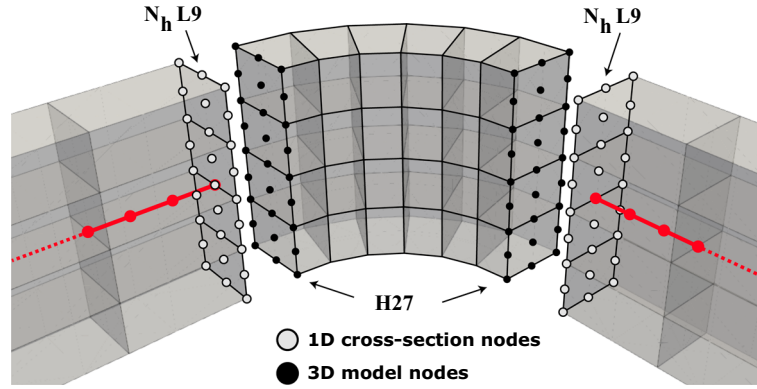
Fig. 7 Clamped angle frame: multi-dimensional discretization adopted

Table 1 Clamped angle frame: convergence analysis, tip horizontal displacement measured at the load point application (mm), comparison between results obtained by 1D+3D CUF models and the reference

Model		$-u_x$ (mm)				
L9/H27	B4	$F = 2.25$ kN	$F = 5.25$ kN	$F = 8.25$ kN	$F = 12.75$ kN	DOF
2L9 + 2x6H27	10	$20.4665^{(4.20\%)}$	$62.3523^{(2.57\%)}$	$90.6258^{(1.71\%)}$	$114.5720^{(1.03\%)}$	3285
	15	$20.4777^{(4.15\%)}$	$62.3722^{(2.54\%)}$	$90.6437^{(1.69\%)}$	$114.5840^{(1.02\%)}$	4635
	20	$20.4823^{(4.13\%)}$	$62.3804^{(2.52\%)}$	$90.6510^{(1.68\%)}$	$114.5885^{(1.02\%)}$	5985
2L9 + 2x8H27	10	$20.4543^{(4.26\%)}$	$62.3288^{(2.61\%)}$	$90.6041^{(1.73\%)}$	$114.5586^{(1.04\%)}$	3465
	15	$20.4653^{(4.20\%)}$	$62.3485^{(2.57\%)}$	$90.6218^{(1.71\%)}$	$114.5704^{(1.03\%)}$	4815
	20	$20.4699^{(4.18\%)}$	$62.3567^{(2.56\%)}$	$90.6290^{(1.70\%)}$	$114.5749^{(1.03\%)}$	6165
4L9 + 4x6H27	10	$21.2387^{(0.58\%)}$	$63.8391^{(0.25\%)}$	$92.1500^{(0.05\%)}$	$115.9014^{(0.12\%)}$	5913
	15	$21.2508^{(0.53\%)}$	$63.8601^{(0.21\%)}$	$92.1687^{(0.03\%)}$	$115.9137^{(0.13\%)}$	8343
	20	$21.2560^{(0.50\%)}$	$63.8691^{(0.20\%)}$	$92.1765^{(0.02\%)}$	$115.9186^{(0.13\%)}$	10773
4L9 + 4x8H27	10	$21.2260^{(0.64\%)}$	$63.8152^{(0.28\%)}$	$92.1282^{(0.08\%)}$	$115.8881^{(0.10\%)}$	6237
	15	$21.2380^{(0.59\%)}$	$63.8361^{(0.25\%)}$	$92.1467^{(0.06\%)}$	$115.9003^{(0.12\%)}$	8667
	20	$21.2431^{(0.56\%)}$	$63.8450^{(0.24\%)}$	$92.1545^{(0.05\%)}$	$115.9051^{(0.12\%)}$	11097
3D ABQ	6000 C8D20R	21.3636	63.9962	92.1986	115.7670	92247

Table 2 Clamped angle frame: convergence analysis, tip vertical displacement measured at the load point application (mm), comparison between results obtained by 1D+3D CUF models and the reference

Model		u_z (mm)				
L9/H27	B4	$F = 2.25$ kN	$F = 5.25$ kN	$F = 8.25$ kN	$F = 12.75$ kN	DOF
2L9 + 2x6H27	10	$105.7439^{(1.34\%)}$	$179.0502^{(1.13\%)}$	$213.6598^{(0.74\%)}$	$242.4510^{(0.52\%)}$	3285
	15	$105.7804^{(1.31\%)}$	$179.0947^{(1.10\%)}$	$213.7070^{(0.72\%)}$	$242.5055^{(0.50\%)}$	4635
	20	$105.7955^{(1.30\%)}$	$179.1128^{(1.09\%)}$	$213.7259^{(0.71\%)}$	$242.5273^{(0.49\%)}$	5985
2L9 + 2x8H27	10	$105.7218^{(1.37\%)}$	$179.0368^{(1.13\%)}$	$213.6566^{(0.74\%)}$	$242.4537^{(0.52\%)}$	3465
	15	$105.7581^{(1.33\%)}$	$179.0812^{(1.11\%)}$	$213.7036^{(0.72\%)}$	$242.5082^{(0.50\%)}$	4815
	20	$105.7732^{(1.32\%)}$	$179.0993^{(1.10\%)}$	$213.7226^{(0.71\%)}$	$242.5300^{(0.49\%)}$	6165
4L9 + 4x6H27	10	$107.4332^{(0.23\%)}$	$180.5947^{(0.27\%)}$	$214.7964^{(0.21\%)}$	$243.2478^{(0.20\%)}$	5913
	15	$107.4721^{(0.27\%)}$	$180.6419^{(0.25\%)}$	$214.8467^{(0.19\%)}$	$243.3065^{(0.17\%)}$	8343
	20	$107.4886^{(0.28\%)}$	$180.6616^{(0.24\%)}$	$214.8674^{(0.18\%)}$	$243.3306^{(0.16\%)}$	10773
4L9 + 4x8H27	10	$107.4108^{(0.21\%)}$	$180.5814^{(0.28\%)}$	$214.7933^{(0.22\%)}$	$243.2506^{(0.20\%)}$	6237
	15	$107.4495^{(0.25\%)}$	$180.6285^{(0.26\%)}$	$214.8435^{(0.19\%)}$	$243.3092^{(0.17\%)}$	8667
	20	$107.4660^{(0.26\%)}$	$180.6482^{(0.25\%)}$	$214.8642^{(0.18\%)}$	$243.3332^{(0.16\%)}$	11097
3D ABQ	6000 C8D20R	107.1850	181.0920	215.2570	243.7270	92247

(a) Global computed equilibrium path

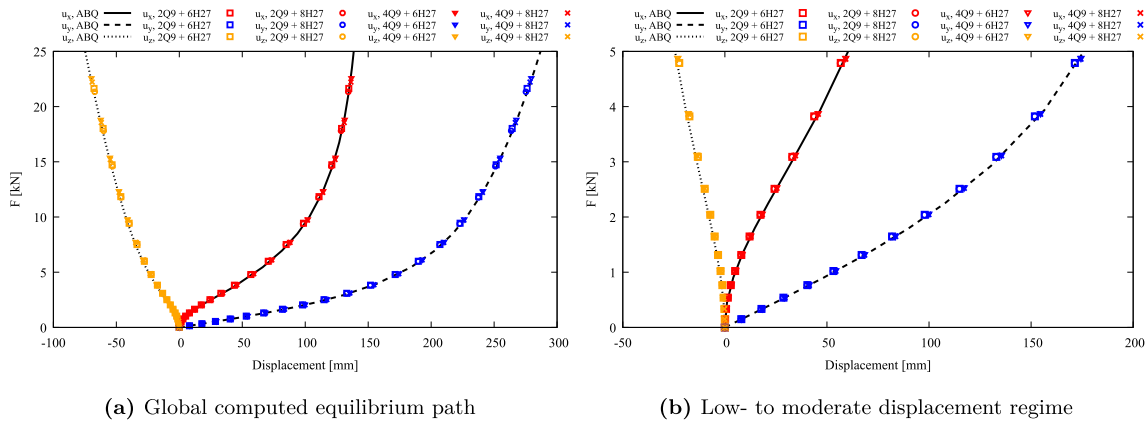(b) Low- to moderate displacement regime

Fig. 8 Clamped angle frame: equilibrium paths

analysis proposed for the transversal displacement component with respect to the load direction, which was computed accurately in all cases.

- Similar percentage differences between the variable-kinematics results and ABAQUS 3D solutions are observed across almost all discretizations considered in both proposed analyses. Results for variable-kinematics models with fewer finite elements along the beam axis also agree. Thus, one can observe that the accuracy is strictly dependent on the cross-section and curved corner discretizations. The proposed coarser discretization ensures computational efficiency but suffers from decreased accuracy. Notably, the $4L9 - 10B4 + 4x6\,H27$ achieves accurate predictions with a 94% reduction in computational costs compared to the reference solutions, with acceptable percentage differences relative to refined models.

4.2 Clamped angle frame

The second case study deals with a clamped angle frame geometrically nonlinear static analyses. Many authors have investigated this benchmark problem in nonlinear static analysis, and in the present work, the case of Zouari et al. [39] has been taken as a reference study case. In the reference, this large deflection problem has been analyzed in its two-dimensional version, considering plane-strain finite element models. The frame is clamped at the left end and subjected to a horizontal force at the top-right end. Figure 9 shows the geometrical features and boundary conditions considered. The frame dimensions are $L = 0.1$ m, $h = 0.01$ m, and thickness $t = 0.01$ m. The mechanical properties are expressed using the Young modulus and Poisson ratio, respectively set to $E = 3 \cdot 10^{11}$ Pa and $\nu = 0.3$, consistently with the nondimensional properties reported in the reference case study. The mathematical models adopted employ unified 1D beam finite element models for the two straight sides of the frame and hexahedral 3D models for the corner. The two square cross-section beams are modeled employing a single L9 element cross-section expansion element and N_{B4} finite elements along the beam axis. The corner is discretized, adopting only one H27 hexahedral parabolic finite element. Figure 9b shows the graphical representation of the discretization adopted. The first numerical investigation is a convergence analysis considering increasing numbers of finite elements along the two straight beams. Tables 3 and 4 show the comparison between displacement components computed by variable-kinematics models when different values of the shear load are considered, comparing the results with a reference solution. In particular, the relative errors between the proposed results and the reference are reported in brackets. Figure 10 shows the equilibrium path at the load point application, obtained adopting N_{B4} B4+1L9 models for each side.

Figure 11 shows the contour of the stress components σ_{xx} and σ_{yy} when $4B4 - 1L9 + 1H27$ is considered as discretization model. The results suggest that

- The convergence analysis shows that the model 2B4+1L9 provided a convergent solution. Minor differences are evidenced in all the cases, but accurate results are obtained in all instances.
- The percentage differences between the proposed results and the reference are under 1% for all the discretization considered. In almost all load conditions, more accurate results are obtained when increasing finite elements along the beam axis are considered.
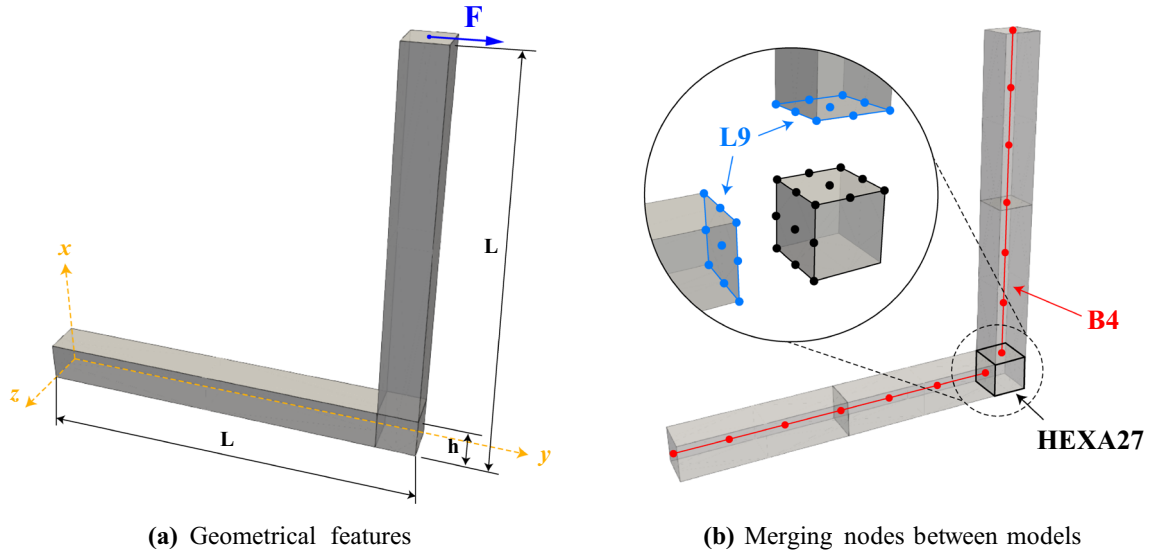
(a) Geometrical features 　　　　　　　　**(b)** Merging nodes between models

Fig. 9 Clamped angle frame: geometry and multi-dimensional discretization adopted

Table 3 Clamped angle frame: convergence analysis, tip horizontal displacement measured at the load point application [mm], comparison between results obtained by 1D+3D CUF models and the reference

F (kN)	$u_{y_{ref}}$ [39]	1 B4	2 B4	4 B4	5 B4	10 B4
4	1.6490	$1.6375^{(-0.695\%)}$	$1.6428^{(-0.374\%)}$	$1.6394^{(-0.584\%)}$	$1.6391^{(-0.602\%)}$	$1.6391^{(-0.598\%)}$
8	2.9820	$2.9600^{(-0.737\%)}$	$2.9664^{(-0.523\%)}$	$2.9615^{(-0.688\%)}$	$2.9611^{(-0.702\%)}$	$2.9612^{(-0.697\%)}$
12	3.9990	$3.9694^{(-0.741\%)}$	$3.9735^{(-0.639\%)}$	$3.9682^{(-0.769\%)}$	$3.9679^{(-0.779\%)}$	$3.9681^{(-0.773\%)}$
16	4.7610	$4.7273^{(-0.708\%)}$	$4.7279^{(-0.696\%)}$	$4.7228^{(-0.802\%)}$	$4.7225^{(-0.808\%)}$	$4.7228^{(-0.803\%)}$
20	5.3330	$5.3001^{(-0.618\%)}$	$5.2973^{(-0.670\%)}$	$5.2925^{(-0.759\%)}$	$5.2923^{(-0.763\%)}$	$5.2926^{(-0.758\%)}$
24	5.7750	$5.7389^{(-0.626\%)}$	$5.7333^{(-0.721\%)}$	$5.7288^{(-0.80\%)}$	$5.7287^{(-0.802\%)}$	$5.7290^{(-0.797\%)}$
28	6.1200	$6.0822^{(-0.617\%)}$	$6.0747^{(-0.741\%)}$	$6.0703^{(-0.812\%)}$	$6.0702^{(-0.813\%)}$	$6.0705^{(-0.808\%)}$
32	6.3950	$6.3561^{(-0.609\%)}$	$6.3471^{(-0.749\%)}$	$6.3429^{(-0.815\%)}$	$6.3429^{(-0.815\%)}$	$6.3432^{(-0.811\%)}$
36	6.6180	$6.5786^{(-0.595\%)}$	$6.5687^{(-0.744\%)}$	$6.5646^{(-0.807\%)}$	$6.5646^{(-0.807\%)}$	$6.5649^{(-0.803\%)}$
40	6.8030	$6.7625^{(-0.595\%)}$	$6.7522^{(-0.747\%)}$	$6.7480^{(-0.809\%)}$	$6.7480^{(-0.808\%)}$	$6.7483^{(-0.804\%)}$
DOF		243	405	729	891	1701

Table 4 Clamped angle frame: convergence analysis, tip vertical displacement measured at the load point application (mm), comparison between results obtained by 1D+3D CUF models and the reference

F [kN]	$u_{x_{ref}}$ [39]	1 B4	2 B4	4 B4	5 B4	10 B4
4	-0.7860	$-0.7789^{(-0.898\%)}$	$-0.7845^{(-0.185\%)}$	$-0.7827^{(-0.414\%)}$	$-0.7825^{(-0.442\%)}$	$-0.7826^{(-0.438\%)}$
8	-1.6710	$-1.6538^{(-1.028\%)}$	$-1.6639^{(-0.424\%)}$	$-1.6604^{(-0.635\%)}$	$-1.6600^{(-0.660\%)}$	$-1.6601^{(-0.654\%)}$
12	-2.5300	$-2.5043^{(-1.016\%)}$	$-2.5161^{(-0.550\%)}$	$-2.5115^{(-0.732\%)}$	$-2.5109^{(-0.754\%)}$	$-2.5111^{(-0.747\%)}$
16	-3.3040	$-3.2723^{(-0.960\%)}$	$-3.2836^{(-0.618\%)}$	$-3.2784^{(-0.773\%)}$	$-3.2778^{(-0.792\%)}$	$-3.2780^{(-0.786\%)}$
20	-3.9750	$-3.9430^{(-0.804\%)}$	$-3.9527^{(-0.560\%)}$	$-3.9474^{(-0.695\%)}$	$-3.9467^{(-0.711\%)}$	$-3.9470^{(-0.705\%)}$
24	-4.5570	$-4.5197^{(-0.819\%)}$	$-4.5275^{(-0.648\%)}$	$-4.5220^{(-0.768\%)}$	$-4.5214^{(-0.782\%)}$	$-4.5216^{(-0.776\%)}$
28	-5.0540	$-5.0150^{(-0.773\%)}$	$-5.0209^{(-0.655\%)}$	$-5.0154^{(-0.763\%)}$	$-5.0148^{(-0.776\%)}$	$-5.0151^{(-0.770\%)}$
32	-5.4820	$-5.4411^{(-0.746\%)}$	$-5.4454^{(-0.667\%)}$	$-5.4400^{(-0.766\%)}$	$-5.4394^{(-0.777\%)}$	$-5.4397^{(-0.772\%)}$
36	-5.8510	$-5.8094^{(-0.711\%)}$	$-5.8124^{(-0.660\%)}$	$-5.8070^{(-0.751\%)}$	$-5.8064^{(-0.762\%)}$	$-5.8067^{(-0.757\%)}$
40	-6.1720	$-6.1294^{(-0.690\%)}$	$-6.1314^{(-0.657\%)}$	$-6.1261^{(-0.744\%)}$	$-6.1255^{(-0.754\%)}$	$-6.1258^{(-0.749\%)}$
DOF		243	405	729	891	1701

(a) Tip horizontal displacement u_y **(b)** Tip vertical displacement u_x
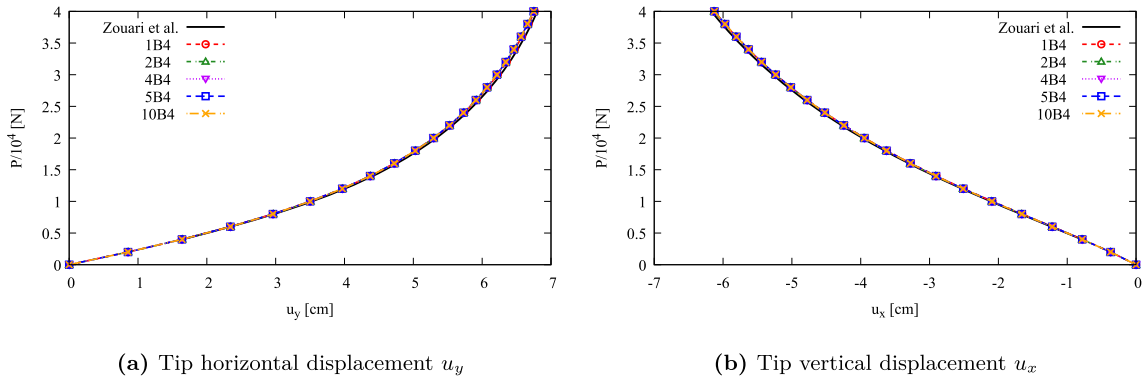
Fig. 10 Clamped angle frame: equilibrium paths

(a) σ_{xx} **(b)** σ_{yy}

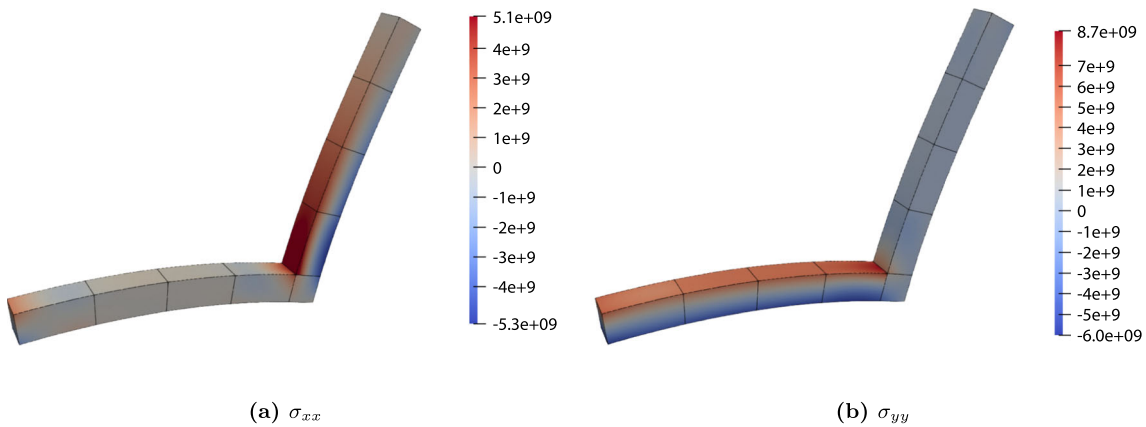**Fig. 11** Clamped angle frame: stress component contours for P = 8.474×10^3 N, stress in Pa

- The proposed variable-kinematics models have proven efficient regarding the computational costs required. A save in terms of DOF of around 85% is registered comparing the 1 B4 model with the 10 B4 model, considered the most accurate one, without any relevant variations of the accuracy.

4.3 Doubly-curved thick beam

The third case study concerns the static analysis of a clamped doubly-curved beam. In the proposed analysis, the mechanical behavior of the frame is investigated in two distinct load conditions. First, a uniform traction tension is applied at the tip-free end along the y-direction. After that, the static nonlinear response is investigated when a transverse shear pressure is applied at the same free end considered before. The frame dimensions are $L = 30$ mm, curvature radius $R = 2$ mm, section height $h = 6$ mm and thickness $t = 3$ mm, and middle span inclination $\theta = 10°$. Figure 12a shows the geometrical features of the analyzed frame, while the boundary conditions and the load case considered are shown in Fig. 12b. The mechanical response of the structure is evaluated by analyzing the displacement components of the point "A" located at the free-end of the frame, as indicated in Fig. 12b. The beam is composed of aluminum, and consequently, its mechanical properties are defined in terms of Young modulus and Poisson ratio, set to $E = 70$ GPa and $\nu = 0.3$, respectively.

The discretization of the whole frame considers CUF 1D beam finite element models or hexahedral 3D models for the two connecting curved regions. The structure has been discretized in two ways concerning the distinct zones. The straight beam-like sub-regions have been discretized adopting 1D CUF models, employing N_y B4 cubic elements along each beam axis and N_E L9 over each beam cross-section. Following the cross-section sub-regions identified by the 1D expansion models, the two curved regions have been discretized considering N_E parabolic H27 elements along the radial direction and N_t H27 elements along the total span. In the following, each discretization adopted will be referred to as N_y B4$-N_E$ L9 + $N_E \times N_t$ H27. Figure 13
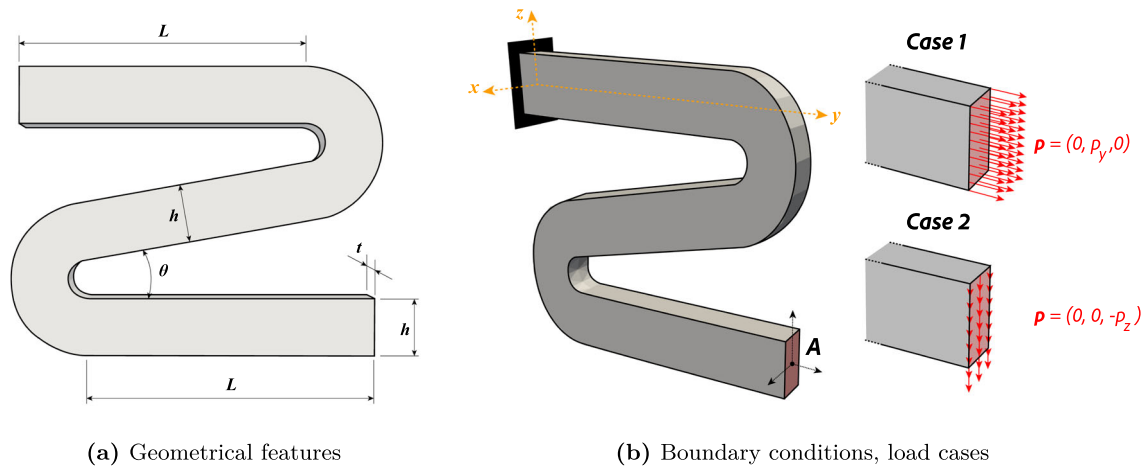
(a) Geometrical features   (b) Boundary conditions, load cases

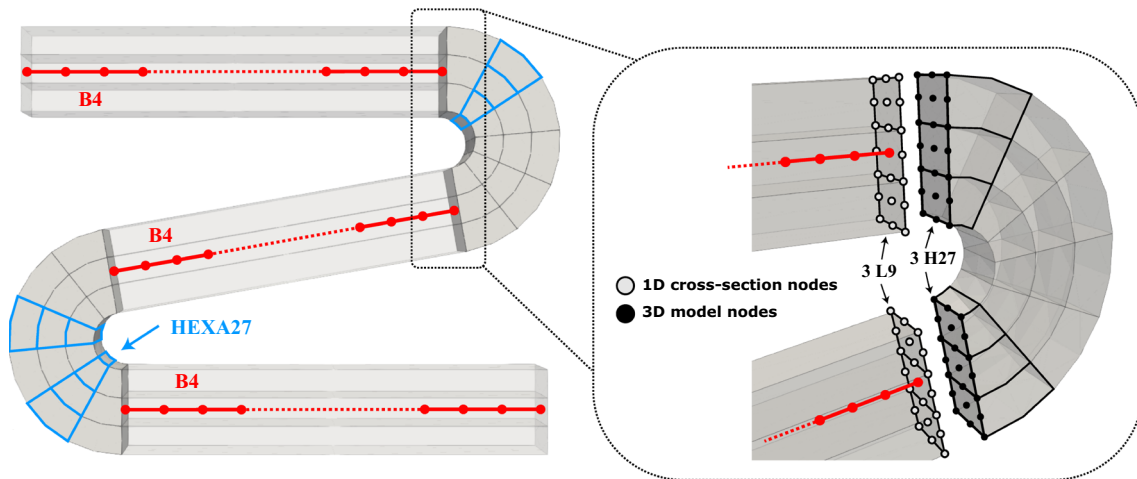**Fig. 12** Doubly-curved thick beam: case study reference description

Fig. 13 Doubly-curved thick beam: multi-dimensional discretization adopted. Example representation of nodes superposition in the case of 3 L9 cross-section expansion elements and corresponding 3 hexahedral elements along the radial direction of the curved frame

shows the discretization technique adopted and the variable-kinematics nodes merging procedure, achieved in correspondence of overlapping surfaces and corresponding nodes between different finite element models. The numerical solutions obtained adopting higher-order variable-kinematics models are compared with the reference solution obtained by ABAQUS 3D models. The effects of the mathematical models adopted on the mechanical response of the structure are investigated. A convergence analysis is carried out, analyzing the displacement components of point "A" with different discretization, considering the increasing number of beam and hexahedral elements. Table 5 compares the numerical results obtained via variable-kinematics discretization models and the full ABAQUS 3D reference solutions. In particular, for three different load conditions, the values of the horizontal u_y and vertical u_z displacement components measured at the point "A" are reported, analyzing the influence of the mathematical model adopted. The percentage difference between the proposed 1D-3D CUF results and the full 3D solution is also in brackets.

The shear pressure load case is considered in Table, 6, with displacements measured again at point "A". The whole equilibrium paths are then computed to analyze the global behavior of the structure on a broader load range. Figures 14 and 15 show the equilibrium curve of the frame when a normal traction pressure is applied, considering the horizontal and vertical displacement components of the point "A" separately. The same results are reported in Figs. 16 and 17 regarding the analysis of a shear traction pressure applied at the free end of the frame. Figures 18 and 19 show the contour plots of normal and transverse σ_{yy} and σ_{yz} stress components when the structure is subjected to a normal pressure of $p = 900$ MPa, comparing the stress distributions obtained

Table 5 Doubly-curved thick beam under traction pressure: horizontal u_z and vertical u_y displacements components (mm)

B4	Model	$p = 900$ MPa		$p = 1650$ MPa		$p = 2400$ MPa		DOF
		u_y	u_z	u_y	u_z	u_y	u_z	
2	2 L9 + 4x2 H27	$52.767^{(1.98\%)}$	$20.466^{(0.27\%)}$	$62.830^{(3.38\%)}$	$22.784^{(0.20\%)}$	$67.639^{(4.32\%)}$	$23.502^{(0.20\%)}$	1575
	2 L9 + 6x2 H27	$52.844^{(1.84\%)}$	$20.470^{(0.29\%)}$	$62.881^{(3.30\%)}$	$22.785^{(0.20\%)}$	$67.679^{(4.27\%)}$	$23.501^{(0.21\%)}$	1935
	3 L9 + 4x3 H27	$52.836^{(1.85\%)}$	$20.176^{(1.15\%)}$	$62.837^{(3.37\%)}$	$22.642^{(0.83\%)}$	$67.603^{(4.37\%)}$	$23.421^{(0.55\%)}$	2205
	3 L9 + 6x3 H27	$52.913^{(1.71\%)}$	$20.180^{(1.13\%)}$	$62.887^{(3.29\%)}$	$22.643^{(0.82\%)}$	$67.642^{(4.32\%)}$	$23.421^{(0.55\%)}$	2709
5	2 L9 + 4x2 H27	$52.755^{(2.00\%)}$	$20.451^{(0.20\%)}$	$62.823^{(3.39\%)}$	$22.766^{(0.28\%)}$	$67.635^{(4.33\%)}$	$23.486^{(0.27\%)}$	2790
	2 L9 + 6x2 H27	$52.833^{(1.86\%)}$	$20.455^{(0.22\%)}$	$62.875^{(3.31\%)}$	$22.768^{(0.27\%)}$	$67.675^{(4.27\%)}$	$23.487^{(0.26\%)}$	3150
	3 L9 + 4x3 H27	$52.822^{(1.88\%)}$	$20.179^{(1.13\%)}$	$62.827^{(3.38\%)}$	$22.642^{(0.82\%)}$	$67.598^{(4.38\%)}$	$23.420^{(0.55\%)}$	3609
	3 L9 + 6x3 H27	$52.901^{(1.73\%)}$	$20.184^{(1.11\%)}$	$62.879^{(3.30\%)}$	$22.644^{(0.81\%)}$	$67.638^{(4.33\%)}$	$23.421^{(0.55\%)}$	4410
10	2 L9 + 4x2 H27	$52.754^{(2.01\%)}$	$20.448^{(0.18\%)}$	$62.821^{(3.39\%)}$	$22.764^{(0.29\%)}$	$67.632^{(4.33\%)}$	$23.485^{(0.27\%)}$	4815
	2 L9 + 6x2 H27	$52.832^{(1.86\%)}$	$20.453^{(0.20\%)}$	$62.873^{(3.31\%)}$	$22.766^{(0.28\%)}$	$67.672^{(4.28\%)}$	$23.486^{(0.27\%)}$	5175
	3 L9 + 4x3 H27	$52.821^{(1.88\%)}$	$20.179^{(1.14\%)}$	$62.826^{(3.39\%)}$	$22.642^{(0.82\%)}$	$67.597^{(4.38\%)}$	$23.420^{(0.55\%)}$	6741
	3 L9 + 6x3 H27	$52.900^{(1.73\%)}$	$20.184^{(1.11\%)}$	$62.878^{(3.31\%)}$	$22.644^{(0.82\%)}$	$67.637^{(4.33\%)}$	$23.421^{(0.55\%)}$	7245
ABQ	1140 C3D20R	53.833	20.411	65.028	22.830	70.696	23.549	21249

Comparison between variable-kinematics discretization model and ABAQUS 3D reference solutions for different load conditions

Table 6 Doubly-curved thick beam under shear pressure: horizontal u_z and vertical u_y displacements components (mm)

B4	Model	$p = 500$ MPa		$p = 1000$ MPa		$p = 1500$ MPa		DOF
		$-u_y$	$-u_z$	$-u_y$	$-u_z$	$-u_y$	$-u_z$	
2	2 L9 + 4x2 H27	$18.666^{(1.28\%)}$	$40.510^{(1.81\%)}$	$21.208^{(0.48\%)}$	$56.567^{(2.94\%)}$	$23.146^{(0.15\%)}$	$65.563^{(3.82\%)}$	1575
	2 L9 + 6x2 H27	$18.659^{(1.32\%)}$	$40.600^{(1.59\%)}$	$21.205^{(0.49\%)}$	$56.643^{(2.81\%)}$	$23.146^{(0.15\%)}$	$65.623^{(3.73\%)}$	1935
	3 L9 + 4x3 H27	$18.664^{(1.29\%)}$	$40.582^{(1.64\%)}$	$21.211^{(0.46\%)}$	$56.631^{(2.83\%)}$	$23.153^{(0.18\%)}$	$65.613^{(3.75\%)}$	2205
	3 L9 + 6x3 H27	$18.657^{(1.33\%)}$	$40.672^{(1.42\%)}$	$21.208^{(0.48\%)}$	$56.707^{(2.70\%)}$	$23.153^{(0.18\%)}$	$65.672^{(3.66\%)}$	2709
5	2 L9 + 4x2 H27	$18.674^{(1.24\%)}$	$40.510^{(1.81\%)}$	$21.233^{(0.36\%)}$	$56.577^{(2.92\%)}$	$23.217^{(0.46\%)}$	$65.619^{(3.74\%)}$	2790
	2 L9 + 6x2 H27	$18.665^{(1.29\%)}$	$40.599^{(1.60\%)}$	$21.228^{(0.38\%)}$	$56.652^{(2.79\%)}$	$23.214^{(0.45\%)}$	$65.678^{(3.65\%)}$	3150
	3 L9 + 4x3 H27	$18.672^{(1.26\%)}$	$40.581^{(1.64\%)}$	$21.235^{(0.35\%)}$	$56.642^{(2.81\%)}$	$23.222^{(0.48\%)}$	$65.670^{(3.66\%)}$	3609
	3 L9 + 6x3 H27	$18.663^{(1.3\%)}$	$40.671^{(1.42\%)}$	$21.230^{(0.38\%)}$	$56.717^{(2.68\%)}$	$23.220^{(0.47\%)}$	$65.729^{(3.58\%)}$	4410
10	2 L9 + 4x2 H27	$18.674^{(1.24\%)}$	$40.509^{(1.81\%)}$	$21.235^{(0.35\%)}$	$56.579^{(2.92\%)}$	$23.230^{(0.52\%)}$	$65.634^{(3.72\%)}$	4815
	2 L9 + 6x2 H27	$18.665^{(1.29\%)}$	$40.599^{(1.60\%)}$	$21.230^{(0.38\%)}$	$56.654^{(2.79\%)}$	$23.227^{(0.51\%)}$	$65.693^{(3.63\%)}$	5175
	3 L9 + 4x3 H27	$18.672^{(1.25\%)}$	$40.581^{(1.64\%)}$	$21.237^{(0.34\%)}$	$56.643^{(2.81\%)}$	$23.235^{(0.54\%)}$	$65.684^{(3.64\%)}$	6741
	3 L9 + 6x3 H27	$18.663^{(1.3\%)}$	$40.670^{(1.42\%)}$	$21.231^{(0.37\%)}$	$56.718^{(2.68\%)}$	$23.233^{(0.53\%)}$	$65.743^{(3.56\%)}$	7245
ABQ	1140 C3D20R	18.909	41.257	21.310	58.278	23.111	68.167	21249

Comparison between variable-kinematics discretization model and ABAQUS 3D reference solutions for different load conditions

via 10B4−3L9 + 6x3 H27 and the ABAQUS 3D solution. A similar comparison is proposed in Figs. 20 and 21 where the contour plots of normal σ_{yy} and σ_{zz} stress components are proposed, considering the frame subjected to a shear pressure of $p = 500$ MPa and discretized with the same model indicated previously. The results suggest that:

- The convergence analysis proposed for the traction pressure case showed that accurate vertical displacement component u_z predictions are obtained for each adopted mathematical model. Moderate discrepancies, less than 5%, are observed for the horizontal displacement component u_y, increasing as the load value increases. Similar considerations are addressed regarding the convergence analysis proposed for the transversal displacement component with respect to the load direction, which was computed accurately in all cases. On the other hand, the discretization model affects the transversal displacement component, but accuracy decreases when the pressure increases.
- In both proposed analyses, similar absolute percentage difference values between variable-kinematics results and ABAQUS 3D solutions are observed in almost all the discretization considered. Results are also in good agreement for variable-kinematics models with fewer finite elements along the beam axis. The predictions obtained via variable-kinematic models are not affected by the total number of finite elements along the beam axis. However, they show sensibility to the cross-section discretization, consequently on the discretization along the radial and tangential directions of the curved corner. The coarser discretization proposed has guaranteed comparable accuracy and efficiency in the required computational costs. Good
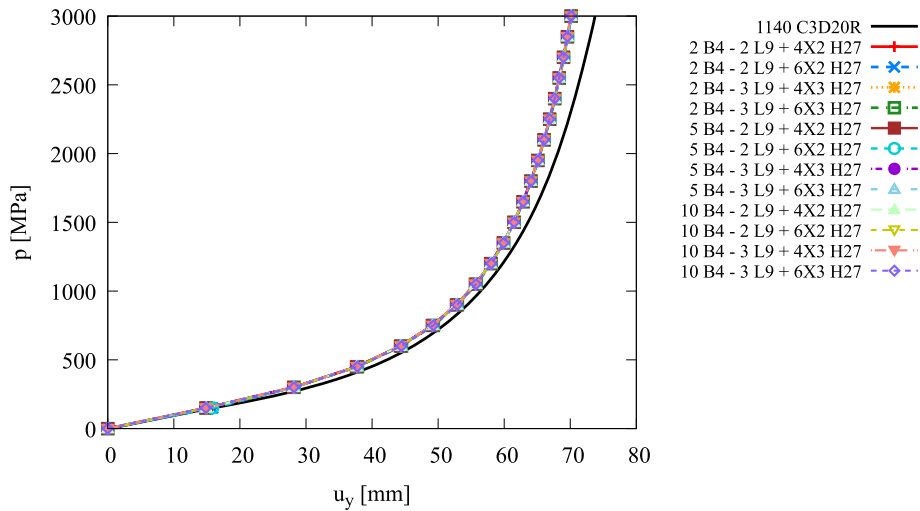
Fig. 14 Doubly-curved thick beam, normal traction pressure case, $\mathbf{p} = (0, p_y, 0)$: equilibrium curve, horizontal displacement vs pressure applied
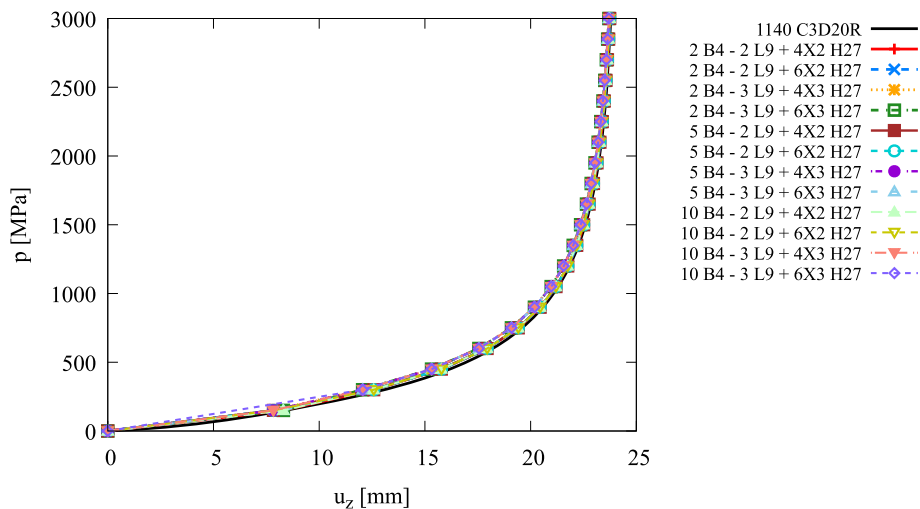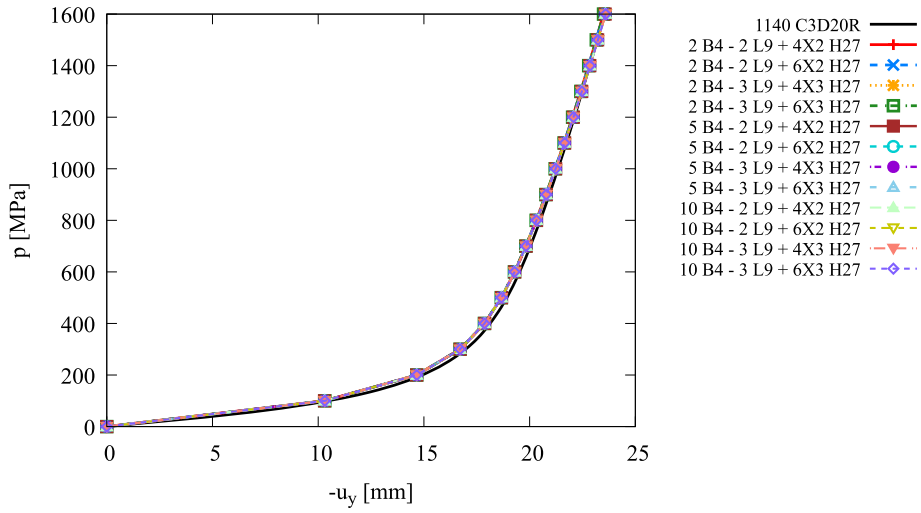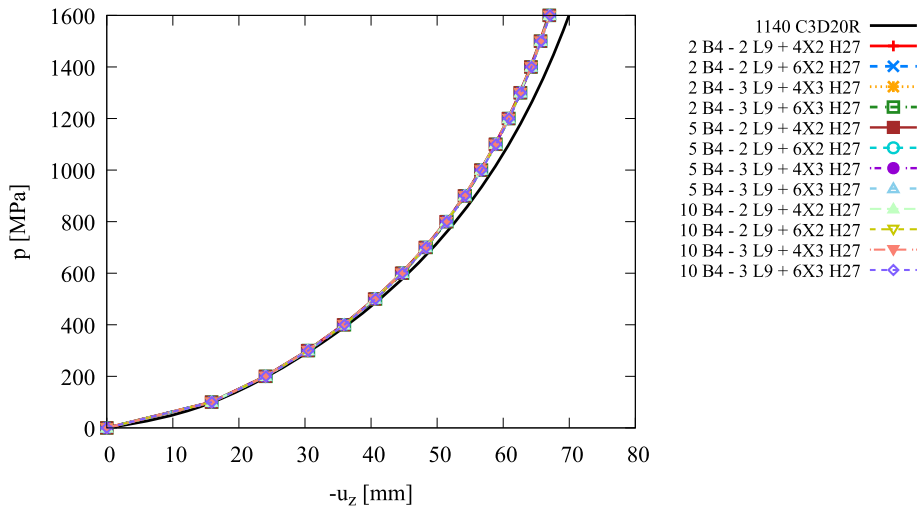

Fig. 15 Doubly-curved thick beam, normal traction pressure case, $\mathbf{p} = (0, p_y, 0)$: equilibrium curves, vertical displacement vs pressure applied

predictions are obtained already with the $2B4-2L9 + 4 \times 2$ H27 model, for which a reduction of 92% in terms of computational costs concerning the reference solutions is observed, and percentage differences are acceptable concerning refined models.

• Stress contour plots show a good agreement with the reference solution. Smooth stress distributions are computed, and local stress concentrations corresponding to the curved corner are coherently predicted. Discrepancies are observed in the case of traction and shear pressure loads or in the computation of stress components, attributed to the different mathematical models adopted in the two numerical models and the local effects arising from the coupling of different structural theories in the corners.

• The 3D solid model is less stiff than the variable-kinematic models proposed; thus, larger displacements are observed. This behavior has also been investigated by the authors in other works [32]. The reason is the different 3D discretization of the corners. The reference 3D model has a finer mesh at the corners. Even if the behavior of the displacement components does not match the complete 3D solution perfectly, low relative percentage differences are observed, under 5%, which is a considerable and reasonable result given that this difference arises at very large displacements.

Fig. 16 Doubly-curved thick beam, shear traction pressure case, $\mathbf{p} = (0, 0, -p_z)$: equilibrium curve, horizontal displacement vs pressure applied

Fig. 17 Doubly-curved thick beam, shear traction pressure case, $\mathbf{p} = (0, 0, -p_z)$: equilibrium curves, vertical displacement vs pressure applied
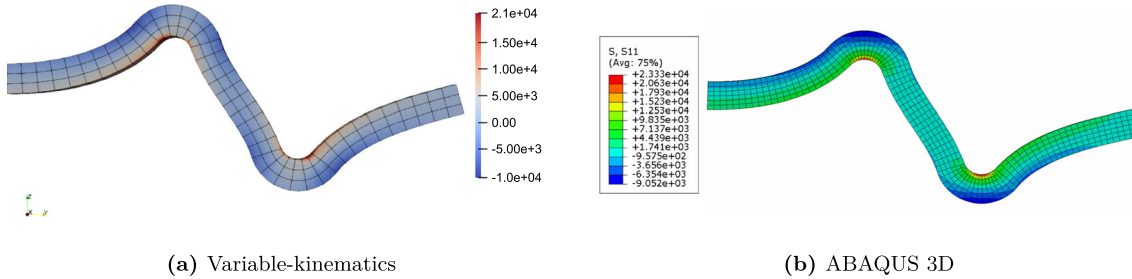

(a) Variable-kinematics   (b) ABAQUS 3D

Fig. 18 Doubly-curved thick beam under traction pressure: contour plot of σ_{yy} stress component for $p = 900$ MPa, stress values in MPa. Comparison between variable-kinematic results and ABAQUS 3D solutions
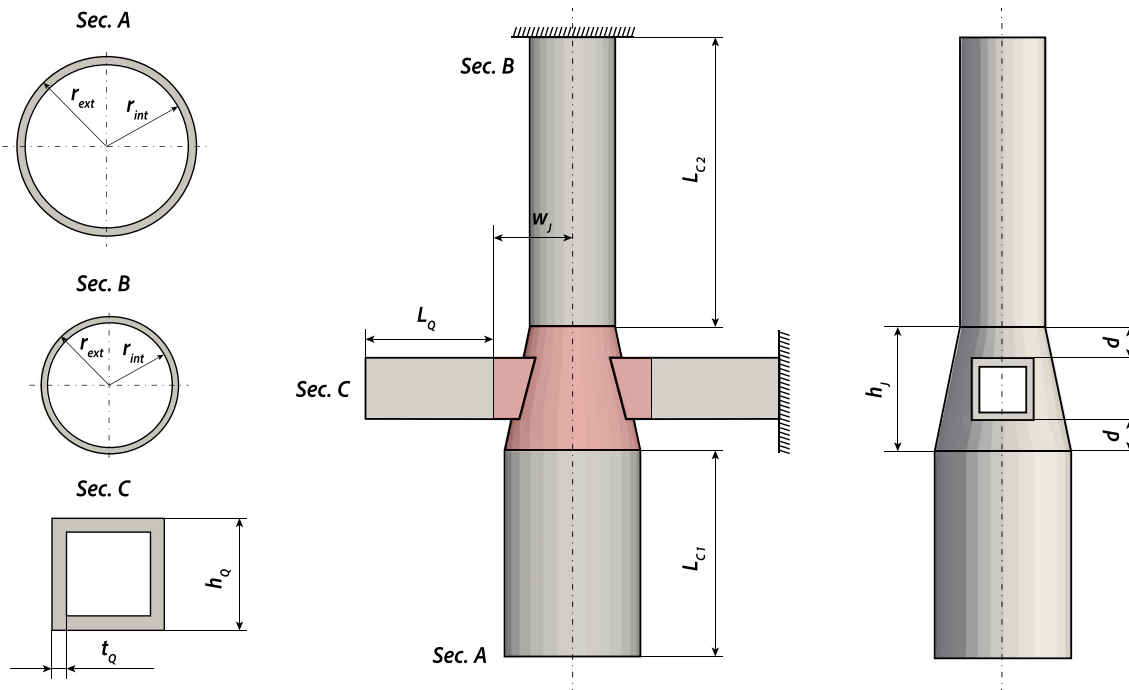
(a) Variable-kinematics   (b) ABAQUS 3D

Fig. 19 Doubly-curved thick beam under traction pressure: contour plot of σ_{yz} stress component for $p = 900$ MPa, stress values in MPa. Comparison between variable-kinematic results and ABAQUS 3D solutions

(a) Variable-kinematics   (b) ABAQUS 3D

Fig. 20 Doubly-curved thick beam under shear pressure: contour plot of σ_{yy} stress component for $p = 500$ MPa, stress values in MPa. Comparison between variable-kinematic results and ABAQUS 3D solutions

(a) Variable-kinematics   (b) ABAQUS 3D
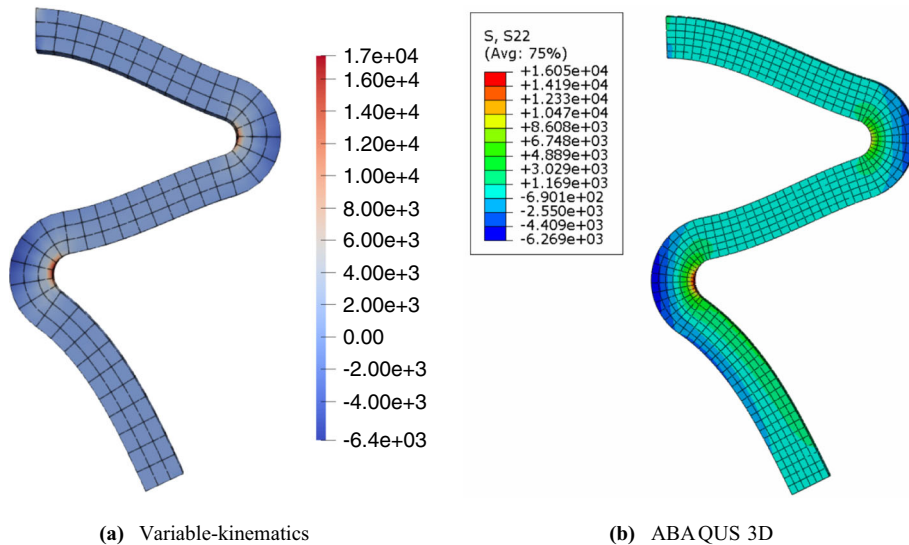
Fig. 21 Doubly-curved thick beam under shear pressure: contour plot of σ_{zz} stress component for $p = 500$ MPa, stress values in MPa. Comparison between variable-kinematic results and ABAQUS 3D solutions

Fig. 22 Pipe joint: geometrical features and boundary conditions considered

Table 7 Pipe joint: dimensions of each sub-components

Sec. A		Sec. B		Sec. C		Joint	
l_{C1}	40 mm	l_{C2}	56 mm	l_Q	23 mm	h_J	24 mm
r_{ext}	13.2 mm	r_{ext}	8.2 mm	h_Q	12 mm	d	6 mm
r_{ext}	12 mm	r_{ext}	7 mm	t_Q	1.5 mm	w_J	17 mm

4.4 Pipe joint structure

The last case study investigates the geometrically nonlinear static analyses of a simplified pipe system connected with a central joint. This case study shows the capabilities of multi-dimensional finite element modeling, adopting classical hexahedral finite elements for connecting zones and refined higher-order beam models. In the global symmetric frame, a joint connects two horizontal hollow square cross-section beams and two vertical cylindrical hollow beams with different internal and external radii. Figure 22 shows each beam frame's geometry, cross-section visualization, and boundary conditions. The dimensions of each beam and connecting joint are listed in Table 7. The whole frame under analysis is made of steel, for which Young modulus and Poisson ratio are $E = 210$ GPa and $\nu = 0.3$. The mathematical model adopted in the 3D joint discretization (the red-colored zone) employs only hexahedral parabolic 3D H27 finite elements. The lateral square cross-section beams adopt refined beam models with 20 parabolic L9 (nine-node) cross-section elements and five cubic B4 elements along the beam axis. Cylindrical beams are modeled employing 30 L9 models for the circular cross-section and ten cubic finite elements along the beam axis. The graphical representation of the mathematical models adopted in the discretization and the connecting zone, allowed by the use of LE models, is depicted in Fig. 23. Figure 24 shows the load conditions applied, considering four F concentrated forces at the free end of the cylindrical beam and eight F/2 concentrated loads at the free end of the hollow square beam. Also, results are expressed in terms of displacement components of the point "A" represented in the same figure, located at coordinate $(0, L_{C_1} + h_J + L_{C_2}, r_{ext_A})$.

Figure 25 shows the equilibrium curves of the structure, specifically showcasing the displacement of point "A" as indicated in Fig. 24. These curves represent the structure's response to incremental increases in the shear load applied at the circular tip-free end of the frame. This figure compares the linear and nonlinear curves in detail, revealing notable discrepancies, particularly for shear loads exceeding 6 kN. By referring to the same
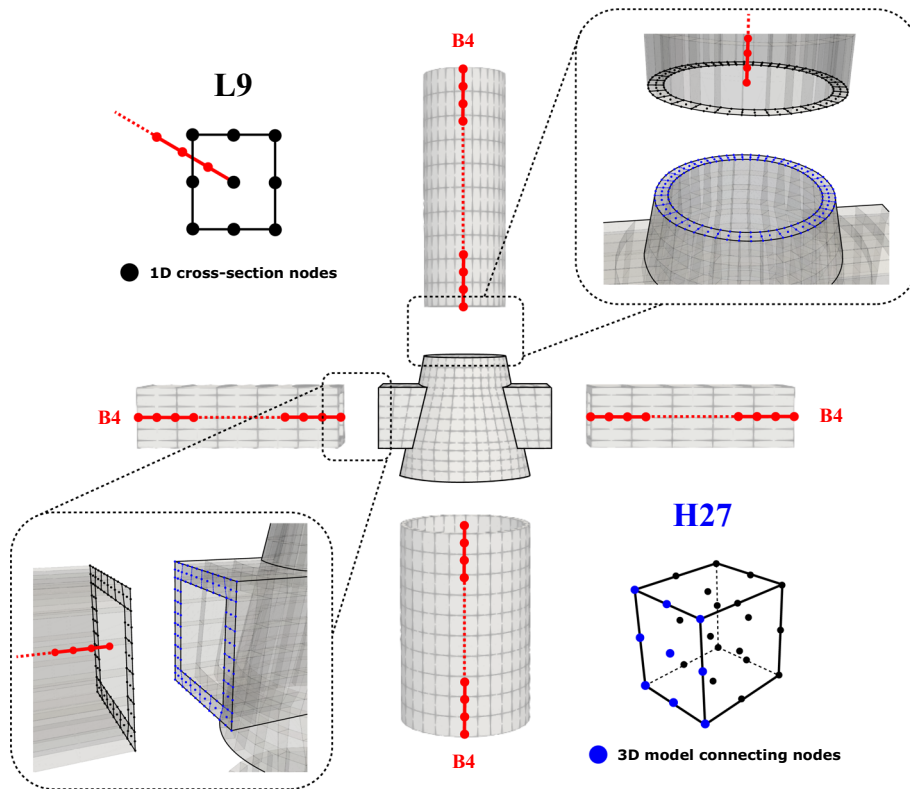
Fig. 23 Pipe joint: multi-dimensional discretization modeling adopted and variable-kinematics models assembling
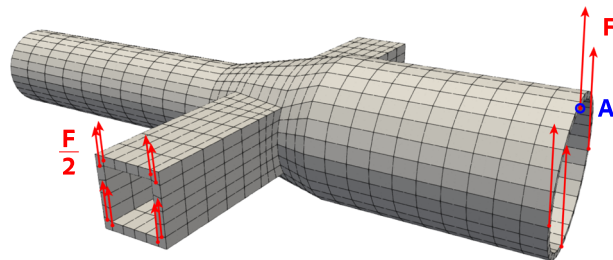

Fig. 24 Pipe joint: reference frame and load conditions

figure, the specific values of displacement components at equilibrium conditions marked are reported explicitly in Table 8, in which the computational cost required by the simulation, in terms of DOF, is reported. Within the moderate load range, the structure exhibits an almost linear behavior.

However, beyond this range, local effects, such as localized buckling of the cylindrical clamped frame, become apparent near the 9–10 kN range. These local effects are shown in Fig. 26a, which depicts the deformed structure in two non-trivial equilibrium states. Additionally, Fig. 27 provides a contour plot of stress components of the joint frame when considering the post-buckling configuration with a shear load value of $F = 10.14$ kN. The global equilibrium path shows a highly nonlinear static response to the applied loads. Notably, typical buckling behavior is observed at the computed critical load of $F = 9.20$ kN, where slight variations in the applied load result in significant increases in displacement components. The highest stress values exceed the linear elastic thresholds, and material nonlinearities should be considered. The results suggest that:

- The proposed approach can detect local effects concerning stress distributions and buckling.
- If compared to standard 3D approaches, the computational cost is low given that some 60k DOF were used.
- The CUF-based FE model's independence from kinematic assumptions and structural theory approximations allows for the straightforward discretization of different cross-section beams within the same
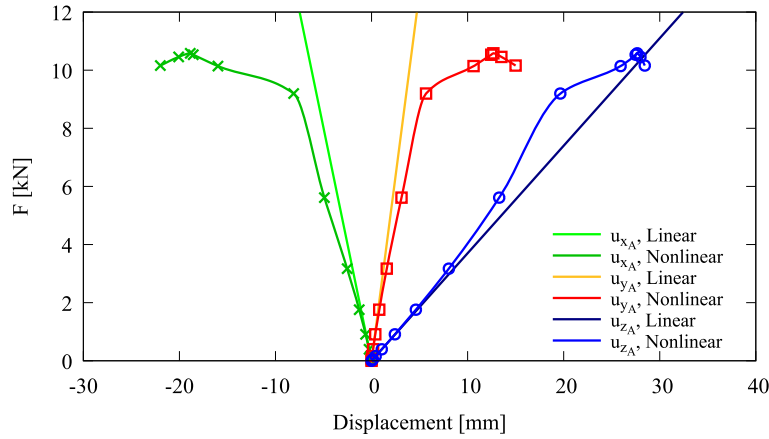
Fig. 25 Pipe joint: multi-dimensional discretization modelling adopted and variable-kinematics models assembling

Table 8 Pipe joint: displacement components measured at the point "A" for different values conditions

Equilibrium conditions							
F (kN)	u_x (mm)	u_y (mm)	u_z (mm)	F (kN)	u_x (mm)	u_y (mm)	u_z (mm)
0.00	0.0000	0.0000	0.0000	5.61	-4.9101	3.1180	13.2871
0.05	-0.0312	0.0197	0.1351	9.20	-8.1083	5.6731	19.6508
0.16	-0.1002	0.0631	0.4284	10.14	-15.9897	10.6175	25.9269
0.40	-0.2558	0.1608	1.0631	10.58	-18.8694	12.6802	27.6567
0.91	-0.6191	0.3880	2.4284	10.16	-21.9841	14.9957	28.4426
1.76	-1.2831	0.8014	4.6121	10.46	-20.0800	13.5115	27.9940
3.17	-2.5373	1.5832	8.0492	10.53	-18.5592	12.4582	27.4918
DOF	60138						

(a) $F = 9196.154$ N

(b) $F = 10140.52$ N
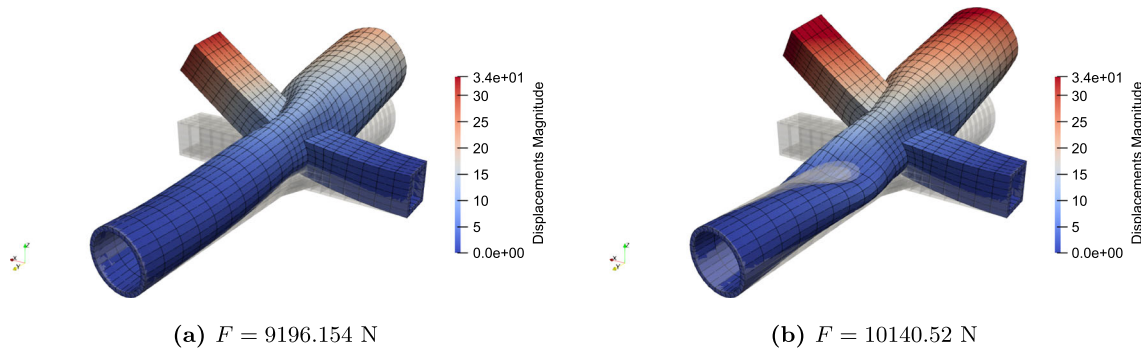
Fig. 26 Pipe joint: deformed configurations for the local buckling representation, displacement in (mm)

environment. By adapting the cross-section expansion discretization to meet the accuracy requirements and discretization constraints necessary for applying the variable-kinematics coupling technique, advanced FE discretization of complex structures can be efficiently implemented.

5 Conclusions

The present work proposes variable-kinematics models based on the unified one-dimensional (1D) beam and three-dimensional (3D) solid finite elements for geometrically nonlinear static and stress analyses of complex structures. Within the well-established Carrera Unified Formulation (CUF) framework, higher-order 1D beam models and classical 3D hexahedral models are defined, resulting in a compact definition of pure displacement-based finite element models. Within this framework, governing equations have been written in terms of Fundamental Nuclei (FN) in a resulting definition of finite element (FE) matrices independent of the theory of
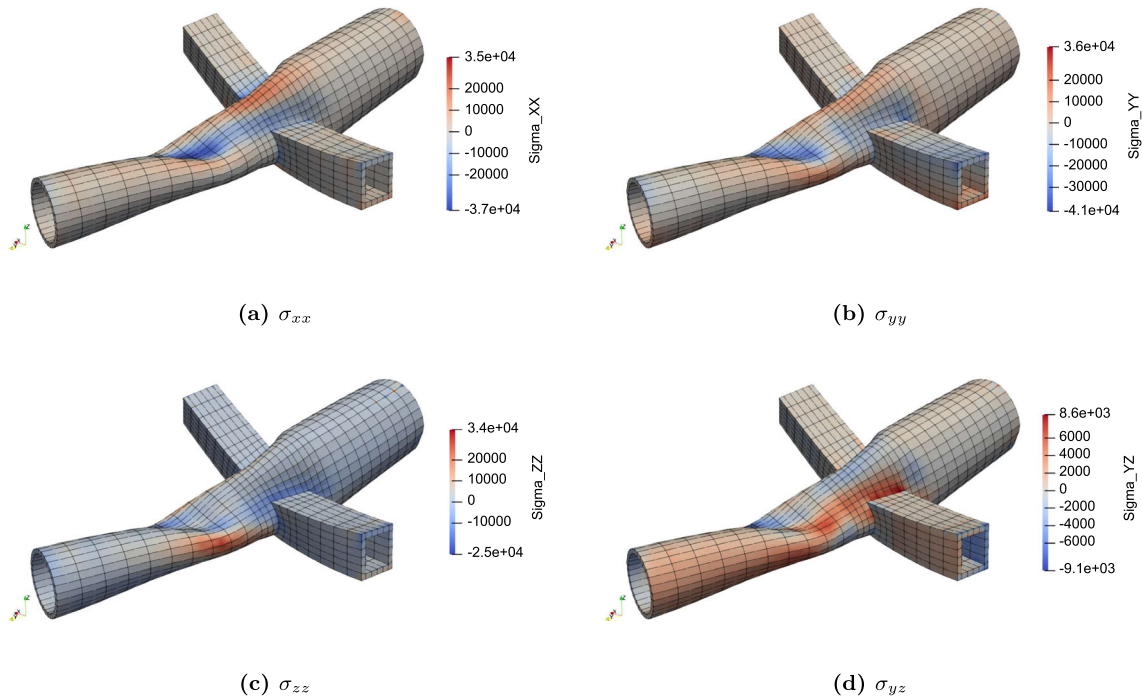
(a) σ_{xx}

(b) σ_{yy}

(c) σ_{zz}

(d) σ_{yz}

Fig. 27 Pipe joint: plot contour of stress components for $F = 10.14$ kN, stress in (MPa)

structure approximation and kinematic models of the displacement field. The proposed multi-dimensional coupling technique has been derived from the definition of the geometrically nonlinear problem in terms of FN. The adoption of higher-order theories allows the analysis of complex mechanical responses, overcoming the limitations of classical beam theories and FE formulations regarding modeling complex mechanical behavior such as cross-section kinematics and localized buckling, with a straightforward coupling technique with the standard 3D FE models, thanks to the CUF framework. The following conclusions can be drawn:

- The present approach proved reliable for various structural configurations, namely a clamped frame, curved beams, and pipes. The coupling between higher-order 1D models and 3D elements provided high accuracy.
- Global and local mechanical responses were detected. Variable-kinematics models were adopted for predicting a highly nonlinear mechanical response, proving local phenomena prediction and local stress concentrations.
- The discretization based on enriched kinematics proved to be efficient concerning computational costs with accuracy similar to the adoption of fully 3D models.

Future works will deal with the variable-kinematics modeling of complex structures for rotodynamic analyses, finite element modeling of soft biological systems in the hyperelastic framework, and the generalization of this coupling technique for shell-like and composite structures. Moreover, to address compatibility requirements at interfaces discussed in the previous section, future works will consider the Node-Dependent Kinematics (NDK) [40,41] technique to analyze complex structures adopting different structural theories node-wise.

Declarations

Conflict of interest The authors have no relevant financial or non-financial interests to disclose.

References

1. Pagani, A., Racionero Sánchez-Majano, A., Zamani, D., Petrolo, M., Carrera, E.: Fundamental frequency layer-wise optimization of tow-steered composites considering gaps and overlaps. Aerotecnica Missili & Spazio (2024)
2. Zienkiewicz, O.C., Taylor, R.L.: The Finite Element Method for Solid and Structural Mechanics. Elsevier, Oxford (2005)
3. Bathe, K.J.: Finite element method. Wiley Encyclopedia of Computer Science and Engineering, pp. 1–12 (2007)
4. Reddy, J.N.: Introduction to the Finite Element Method. McGraw-Hill Education, New York (2019)
5. Euler, L.: De Curvis Elasticis. Geneva (1774)
6. Timoshenko, S.P.: On the corrections for shear of the differential equation for transverse vibration of prismatic bars. Philos. Mag. **41**, 744–746 (1922)
7. Love, A.E.H.: The small free vibrations and deformation of a thin elastic shell. Philos. Trans. R. Soc. Lond. A **179**, 491–546 (1888)
8. Reissner, E.: The effect of transverse shear deformation on the bending of elastic plates. ASME J. Appl. Mech. **12**, 68–77 (1945)
9. Mindlin, R.D.: Influence of rotatory inertia and shear on flexural motions of isotropic elastic plates. ASME J. Appl. Mech. **18**, 31–38 (1951)
10. Pagani, A., Azzara, R., Augello, R., Carrera, E.: Stress states in highly flexible thin-walled composite structures by unified shell model. AIAA J. **59**(10), 4243–4256 (2021). https://doi.org/10.2514/1.J060024
11. Hui, Y., Giunta, G., De Pietro, G., Belouettar, S., Carrera, E., Huang, Q., Liu, X., Hu, H.: A geometrically nonlinear analysis through hierarchical one-dimensional modelling of sandwich beam structures. Acta Mech. **234**(1), 67–83 (2022). https://doi.org/10.1007/s00707-022-03194-7
12. Zhen, W., Jie, M., Shengbo, L., Xiaohui, R.: Five-variable higher-order model for accurate analysis and design of laminated plates. Acta Mech. **235**(5), 3073–3093 (2024). https://doi.org/10.1007/s00707-024-03875-5
13. Argyris, J.H., Kelsey, S.: Energy Theorems and Structural Analysis, vol. 60. Springer, New York (1960)
14. Surana, K.S.: Geometrically non-linear formulation for the three dimensional solid-shell transition finite elements. Comput. Struct. **15**(5), 549–566 (1982)
15. Liao, C.L., Reddy, J.N., Engelstad, S.P.: A solid-shell transition element for geometrically non-linear analysis of laminated composite structures. Int. J. Numer. Meth. Eng. **26**(8), 1843–1854 (1988)
16. Cofer, W.F., Will, K.M.: A three-dimensional, shell-solid transition element for general nonlinear analysis. Comput. Struct. **38**(4), 449–462 (1991)
17. Gmür, T.C., Kauten, R.H.: Three-dimensional solid-to-beam transition elements for structural dynamics analysis. Int. J. Numer. Meth. Eng. **36**(9), 1429–1444 (1993)
18. McCune, R.W., Armstrong, C.G., Robinson, D.J.: Mixed-dimensional coupling in finite element models. Int. J. Numer. Meth. Eng. **49**(6), 725–750 (2000)
19. Song, H.: Rigorous joining of advanced reduced-dimensional beam models to solid finite element models. Ph.D. thesis, Georgia Institute of Technology (2010)
20. Blanco, P.J., Feijóo, R.A., Urquiza, S.A.: A variational approach for coupling kinematically incompatible structural models. Comput. Methods Appl. Mech. Eng. **197**(17–18), 1577–1602 (2008)
21. Shim, K.W., Monaghan, D.J., Armstrong, C.G.: Mixed dimensional coupling in finite element stress analysis. Eng. Comput. **18**, 241–252 (2002)
22. Robinson, T.T., Armstrong, C.G., Fairey, R.: Automated mixed dimensional modelling from 2D and 3D CAD models. Finite Elem. Anal. Des. **47**(2), 151–165 (2011)
23. Reddy, J.N.: A simple higher-order theory for laminated composite plates. J. Appl. Mech. **51**(4), 745–752 (1984)
24. Sànchez-Majano, A.R., Azzara, R., Pagani, A., Carrera, E.: Accurate stress analysis of variable angle tow shells by high-order equivalent-single-layer and layer-wise finite element models. Materials **14**(21), 6486 (2021)
25. Azzara, R., Carrera, E., Filippi, M., Pagani, A.: Time response stress analysis of solid and reinforced thin-walled structures by component-wise models. Int. J. Struct. Stab. Dyn. **20**(14), 2043010 (2020). https://doi.org/10.1142/S0219455420430105
26. Filippi, M., Azzara, R., Carrera, E.: Rotordynamic analyses with variable-kinematic beam and shell finite elements. Mech. Adv. Mater. Struct. (2023). https://doi.org/10.1080/15376494.2023.2246221
27. Carrera, E., Zappino, E.: Carrera Unified Formulation for free-vibration analysis of aircraft structures. AIAA J. **54**(1), 280–292 (2016). https://doi.org/10.2514/1.J054265
28. Azzara, R., Filippi, M., Carrera, E.: Rotordynamic analyses of stiffened cylindrical structures using high-fidelity shell models. Mech. Adv. Mater. Struct. (2024). https://doi.org/10.1080/15376494.2024.2309655
29. Filippi, M., Zappino, E., Carrera, E., Castanié, Bruno: Effective static and dynamic finite element modeling of a double swept composite rotor blade. J. Am. Helicopter Soc. **65**(3), 1–12 (2020). https://doi.org/10.4050/JAHS.65.032003
30. Scano, D., Carrera, E., Petrolo, M.: Use of the 3d equilibrium equations in the free-edge analyses for laminated structures with the variable kinematics approach. Aerotecnica Missili & Spazio (2023)
31. Pagani, A., Carrera, E.: Unified formulation of geometrically nonlinear refined beam theories. Mech. Adv. Mater. Struct. **25**(1), 15–31 (2016)
32. Pagani, A., Chiaia, P., Filippi, M., Cinefra, M.: Unified three-dimensional finite elements for large strain analysis of compressible and nearly incompressible solids. Mech. Adv. Mater. Struct. (2023)
33. Carrera, E., Cinefra, M., Zappino, E., Petrolo, M.: Finite Element Analysis of Structures Through Unified Formulation. Wiley, Hoboken (2014)

34. Carrera, E., Giunta, G., Petrolo, M.: Beam Structures Classical and Advanced Theories. Wiley, Chichester (2011)
35. Reddy, J.N.: Introduction to Nonlinear Finite Element Analysis With Applications to Heat Transfer, Fluid Mechanics, and Solid Mechanics. Oxford University Press, Oxford (2014)
36. Crisfield, M.A.: An arc-length method including line searches and accelerations. Int. J. Numer. Meth. Eng. **19**(9), 1269–1289 (1983)
37. Wu, B., Pagani, A., Filippi, M., Chen, W.Q., Carrera, E.: Large-deflection and post-buckling analyses of isotropic rectangular plates by Carrera Unified Formulation. Int. J. Non-Linear Mech. **116**, 18–31 (2019)
38. Zappino, E., Carrera, E.: Multidimensional model for the stress analysis of reinforced shell structures. AIAA J. **56**(4), 1647–1661 (2018). https://doi.org/10.2514/1.J056384
39. Zouari, W., Hammadi, F., Ayad, R.: Quadrilateral membrane finite elements with rotational DOFs for the analysis of geometrically linear and nonlinear plane problems. Comput. Struct. **173**, 139–149 (2016). https://doi.org/10.1016/j.compstruc.2016.06.004
40. Carrera, E., Pagani, Augello, R.: Large deflection of composite beams by finite elements with node-dependent kinematics. Comput. Mech. **69**, 1481–1500 (2022)
41. Carrera, E., Pagani, Augello, R.: Large deflection and post-buckling of thin-walled structures by finite elements with node-dependent kinematics. Acta Mech. **232**, 591–617 (2021)